NUCL SCI TECH (2018) 29:164
https://doi.org/10.1007/s41365-018-0504-z

Examining the model dependence of the determination of kinetic freeze-out temperature and transverse flow velocity in small collision system

Hai-Ling Lao[1] · Fu-Hu Liu[1] · Bao-Chun Li[1] · Mai-Ying Duan[1] · Roy A. Lacey[2]

Received: 10 May 2018 / Revised: 28 August 2018 / Accepted: 29 August 2018 / Published online: 4 October 2018

Abstract The transverse momentum distributions of the identified particles produced in small collision systems at the Relativistic Heavy Ion Collider (RHIC) and Large Hadron Collider (LHC) have been analyzed by four models. The first two models utilize the blast-wave model with different statistics. The last two models employ certain linear correspondences based on different distributions. The four models describe the experimental data measured by the Pioneering High Energy Nuclear Interaction eXperiment, Solenoidal Tracker at RHIC, and A Large Ion Collider Experiment collaborations equally well. It is found that both the kinetic freeze-out temperature and transverse flow velocity in the central collisions are comparable with those in the peripheral collisions. With the increase of collision energy from that of the RHIC to that of the LHC, the considered quantities typically do not decrease. Comparing with the central collisions, the proton–proton collisions are closer to the peripheral collisions.

This work was supported by the National Natural Science Foundation of China (Nos. 11575103 and 11747319), the Shanxi Provincial Natural Science Foundation (No. 201701D121005), the Fund for Shanxi "1331 Project" Key Subjects Construction, and the US DOE (DE-FG02-87ER40331.A008).

✉ Fu-Hu Liu
fuhuliu@163.com; fuhuliu@sxu.edu.cn

[1] Institute of Theoretical Physics & State Key Laboratory of Quantum Optics and Quantum Optics Devices, Shanxi University, Taiyuan 030006, China

[2] Departments of Chemistry & Physics, Stony Brook University, Stony Brook, NY 11794, USA

Keywords Kinetic freeze-out temperature · Transverse flow velocity · Small collision system · Central collisions · Peripheral collisions

1 Introduction

As an important concept in both thermal and subatomic physics, temperature is widely used in experimental measurements and theoretical studies. Contrary to macroscopic thermal physics, temperature in microscopic subatomic physics cannot be measured directly; nevertheless, the temperature measured in thermal physics is manifested by the change of a given quantity of the thermometric material. Instead, we can calculate the temperature by using the methods of particle ratios and transverse momentum (p_T) spectra. The temperature obtained from particle ratios is typically the chemical freeze-out temperature (T_{ch}), which can describe the degree of excitation of the interacting system at the stage of chemical equilibrium. The temperature obtained from the p_T spectra with a thermal distribution that does not include the flow effect, is typically an effective temperature (T_{eff} or T), which is not a real temperature due to its relation to the particle mass. The temperature obtained from the p_T spectra with a thermal distribution that includes the flow effect is typically the kinetic freeze-out temperature (T_{kin} or T_0), which describes the degree of excitation of the interacting system at the stage of kinetic and thermal equilibrium.

The chemical freeze-out and kinetic freeze-out are two main stages of the evolution of the interacting system in high-energy collisions. At the stage of chemical freeze-out, the chemical components (relative fractions) of the particles are fixed. At the stage of kinetic freeze-out, the p_T and

momentum (p) spectra of the particles are no longer changed. We are interested in the T_0 value, owing to its relation to the p_T spectrum of the identified particles, which is one of the quantities measured first in our experiments. At the same time, T_0 is related to the structure of the phase diagram in the T_0-related spaces, such as T_0 as a function of β_T and as a function of $\sqrt{s_{NN}}$, where β_T is the mean transverse flow velocity, resulted from the impact and squeeze while $\sqrt{s_{NN}}$ denotes the center-of-mass energy per nucleon pair in collisions of nuclei ($\sqrt{s}$ in particle collisions such as in proton–proton (p–p or pp) collisions). In particular, in the energy ranges available in the beam energy scan (BES) program at the Relativistic Heavy Ion Collider (RHIC) and the BES program at the Super Proton Synchrotron (SPS), the chemical potential (μ_B) of baryons needs to be considered. Then, the structure of phase diagram in the T_0 versus μ_B space can be studied in both the RHIC BES and the SPS BES energy ranges.

Generally, μ_B can be obtained from the particle ratios and its excitation function has been studied in detail [1–5], while T_0 and β_T can be obtained from the p_T spectra. In Refs. [6–13], different methods have been used to obtain T_0 and β_T. In our recent studies [14–17], we have used a number of models to obtain T_0 and β_T in nucleus–nucleus (gold–gold (Au–Au) and lead–lead (Pb–Pb)) collisions at RHIC and Large Hadron Collider (LHC) energies, where the top RHIC energy was $\sqrt{s_{NN}} = 200$ GeV while the LHC energy reached a few TeV. Similar results were obtained when a nonzero β_T was used in peripheral nucleus–nucleus collisions in the blast-wave model with Boltzmann–Gibbs statistics (BGBW model) [6–8, 18] and with Tsallis statistics (TBW model) [9, 18, 19]. Our results show that T_0 (β_T) in central nucleus–nucleus collisions is comparable to that in peripheral collisions. Similarly, the values of T_0 and β_T at the LHC are close to those at the RHIC.

It is interesting to compare the results of different models in small collision systems, such as pp and deuteron–gold (d–Au) collisions at the RHIC, and pp and proton–lead (p–Pb) collisions at the LHC. In this paper, we use four models to obtain T_0 and β_T values from the p_T spectra of the identified particles produced in pp and d–Au collisions at the RHIC, and in pp and p–Pb collisions at the LHC. The model results of the p_T spectra are compared with each other and with the experimental data of the Pioneering High Energy Nuclear Interaction eXperiment (PHENIX) [20], Solenoidal Tracker at RHIC (STAR) [21–23], and A Large Ion Collider Experiment (ALICE) collaborations [24, 25]. Then, similar T_0 and β_T values are obtained from the analyses of the experimental data by the four models.

The paper is structured as follows: The formalism and method are described in Sect. 2, results and discussion are given in Sect. 3, finally, in Sect. 4, we summarize our main observations and conclusions.

2 Formalism and method

In the present work, four models were used for the p_T distributions for comparisons in small collision systems; nevertheless, in our recent work [14] they were employed to obtain T_0 and β_T values in nucleus–nucleus collisions at RHIC and LHC energies using a different superposition of soft excitation and hard scattering components. In order to provide a comprehensive review of the present work, we discuss the previous studies of the four models as follows.

(i) BGBW model [6–8]: In this model, we considered a nonzero β_T of the produced particles. According to Refs. [6–8], the BGBW model gives the p_T distribution as

$$f_1(p_T) = \frac{1}{N}\frac{dN}{dp_T} = C_1 p_T m_T \int_0^R r dr \times I_0\left[\frac{p_T \sinh(\rho)}{T_0}\right] K_1\left[\frac{m_T \cosh(\rho)}{T_0}\right], \quad (1)$$

where N is the number of particles, C_1 is a normalized constant, I_0 and K_1 are modified Bessel functions of the first and second kinds, respectively, $m_T = \sqrt{p_T^2 + m_0^2}$ is the transverse mass, $\rho = \tanh^{-1}[\beta(r)]$ is the boost angle, $\beta(r) = \beta_S(r/R)^{n_0}$ is a self-similar flow profile, β_S is the flow velocity on the surface, r / R is the relative radial position in the thermal source [6], and $n_0 = 2$ similarly to that in Ref. [6]. The relation between β_T and $\beta(r)$ is $\beta_T = (2/R^2)\int_0^R r\beta(r)dr = 2\beta_S/(n_0+2) = 0.5\beta_S$.

(ii) TBW model [9]: In this model, we also considered a nonzero β_T.
According to Ref. [9], the TBW model gives the p_T distribution in the form of

$$f_2(p_T) = \frac{1}{N}\frac{dN}{dp_T} = C_2 p_T m_T \int_{-\pi}^{\pi} d\phi \int_0^R r dr \Big\{1 + \frac{q-1}{T_0}\big[m_T \cosh(\rho) - p_T \sinh(\rho)\cos(\phi)\big]\Big\}^{-q/(q-1)}, \quad (2)$$

where C_2 is a normalized constant, q is an entropy index characterizing the degree of non-equilibrium, ϕ denotes the azimuth [9], and $n_0 = 1$ similarly to that in Ref. [9]. In the first two models n_0 is independent: it does not matter if $n_0 = 1$ or $n_0 = 2$ is used. To be compatible with Refs. [6]

and [9], we use $n_0 = 2$ in the first model and $n_0 = 1$ in the second model. It should be noted that we use the index $-q/(q-1)$ in Eq. (2) instead of $-1/(q-1)$ in Ref. [9] due to the fact that q is very close to one. This substitution results in a small and negligible difference in the Tsallis distribution [19].

(iii) An alternative method, in which the intercept in the T versus m_0 relation is assumed to be T_0 [7, 10–13], the slope in the $\langle p_T \rangle$ versus $\overline{m}$ relation is assumed to be β_T, and the slope in the $\langle p \rangle$ versus $\overline{m}$ relation is assumed to be the radial flow velocity β [14–17], which does not include the contribution of longitudinal flow. Here, m_0 denotes the rest mass, $\overline{m}$ denotes the mean moving mass (mean energy), $\langle \cdots \rangle$ denotes the theoretical distribution average of the considered quantity, and T is obtained from a Boltzmann distribution [18]. Two steps are required to obtain T_0 and β_T. To use the relations $T = T_0 + am_0$, $\langle p_T \rangle = b_1 + \beta_T \overline{m}$, and $\langle p \rangle = b_2 + \beta \overline{m}$, where a, b_1, and b_2 are fitted parameters, we choose the form of Boltzmann distribution as [18]

$$f_3(p_T) = \frac{1}{N}\frac{dN}{dp_T} = C_3 p_T m_T \exp\left(-\frac{m_T}{T}\right), \quad (3)$$

where C_3 is a normalized constant related to the free parameter T and particle mass m_0 via its relation to m_T; nevertheless, the Boltzmann distribution has multiple forms [18].

(iv) This model is similar to the third model, but T is obtained from a Tsallis distribution [18, 19]. We choose the Tsallis distribution in the form of [18, 19]

$$f_4(p_T) = \frac{1}{N}\frac{dN}{dp_T} = C_4 p_T m_T \left(1 + \frac{q-1}{T} m_T\right)^{-q/(q-1)}, \quad (4)$$

where C_4 is a normalized constant related to the free parameters T and q, as well as m_0; nevertheless, the Tsallis distribution has more than one forms [18, 19].

Similarly to our recent work [14], in both the BGBW and TBW models, a nonzero β_T of the produced particles is considered in the peripheral nucleus–nucleus collisions. The peripheral collisions contain a small number of participant nucleons that take part in the violent interactions. This condition is similar to a small collision system, which also contains a small number of participant nucleons. When the cold nuclear effect is neglected, the small collision system is similar to a peripheral collisions. This means that a non-zero β_T needs to be considered for the small collision system to maintain consistency; however, the values of β_T for a small collision system and peripheral collisions are possibly different. Naturally, it is not unusual if the values of β_T in the two types of collisions are nearly the same.

From the first model T_0 and β_T can be obtained, while from the second model T_0, β_T, and q can be obtained. The first two models are employed to compare their results. Although the forms of the first two models are obviously different, the values of T_0 (β_T) obtained from them exhibit a little difference only. The last two models are used for comparison as well. The obtained values of the last two models exhibit a little difference as well; however, they are still noticeably different.

The description of the above models is presented at midrapidity, in which $y \approx 0$, where $y \equiv 0.5 \ln[(E + p_z)/(E - p_z)]$, and E and p_z denote the energy and longitudinal momentum, respectively. At high p_T, $y \approx -\ln\tan(\vartheta/2) \equiv \eta$, where ϑ and η denote the emission angle and pseudorapidity of the considered particle, respectively. The effect of the spin and chemical potential on the p_T spectra is neglected because they are small at the top RHIC and LHC energies [1–4]. Similar to our recent work [14], the kinetic freeze-out temperature, the mean transverse (radial) flow velocity, and the effective temperature in different models are uniformly denoted by T_0, β_T, and T, respectively; however, different values can be obtained by different models.

Equations (1)–(4) are the functions describing mainly the contribution of the soft excitation process. These are only valid for the spectra in a narrow p_T range, which mainly covers the range of 0 to 2.5–3.5 GeV/c in most cases or a slightly higher in certain cases. Even for the soft excitation process, the Boltzmann distribution is not sufficient to fit the p_T spectra in certain cases. In the case of a two- or three-component Boltzmann distribution, T is the weighted average resulting from different effective temperatures and the corresponding fractions obtained from different components.

Generally, in the present work, two main processes in high-energy collisions are considered. Apart from the soft excitation process, the main process is the hard scattering process, which contributes to the spectra in a wide p_T range and according to the quantum chromodynamics (QCD) calculations [26–28], it can be described by an inverse power law as

$$f_H(p_T) = \frac{1}{N}\frac{dN}{dp_T} = A p_T \left(1 + \frac{p_T}{p_0}\right)^{-n}, \quad (5)$$

where p_0 and n are free parameters, and A is a normalized constant related to the free parameters. As a result of the QCD-based calculation, Eq. (5) contributes to the distribution in a range of 0 to high p_T. Theoretically, in spite of the overlapping regions in the low p_T range between the

contributions of Eqs. (1)–(4) and (5), they cannot replace each other.

The experimental p_T spectra are typically distributed in a wide range. This means that a superposition of both the contributions of soft and hard processes (components) needs to be used to fit the spectra. We use the usual step function for structuring the superposition in order to avoid the entanglement between the contribution ranges of the soft excitation and hard scattering components, such that

$$f_0(p_T) = \frac{1}{N}\frac{dN}{dp_T} = A_1\theta(p_1 - p_T)f_S(p_T) + A_2\theta(p_T - p_1)f_H(p_T), \quad (6)$$

where $f_S(p_T)$ denotes one of Eqs. (1)–(4), A_1 and A_2 are constants, ensuring that the contributions of soft and hard components are the same at $p_T = p_1$, and the step function $\theta(x) = 1$ if $x > 0$ and $\theta(x) = 0$ if $x < 0$. The fraction (rate) of the contribution of the soft component is given by $k = \int_0^{p_1} A_1 f_S(p_T)dp_T$. Owing to the respective ranges of the different contributions, the selection of parameters in Eqs. (1)–(4) and (5) has no effect on their correlation and dependence on each other.

In certain cases, the contribution of the resonance production for pions and the strong stopping effect for the participating nucleons are non-negligible at very low ranges. A very soft component needs to be used for the p_T values ranging from 0 to 0.5–1.5 GeV/c. Let us consider the contribution of the very soft component. Equation (6) can be rewritten as

$$f_0(p_T) = \frac{1}{N}\frac{dN}{dp_T} = A_{VS}\theta(p_{VS} - p_T)f_{VS}(p_T) + A_1\theta(p_T - p_{VS})\theta(p_1 - p_T)f_S(p_T) + A_2\theta(p_T - p_1)f_H(p_T), \quad (7)$$

where $f_{VS}(p_T)$ denotes one of Eqs. (1)–(4) similarly to $f_S(p_T)$, and A_{VS} is a constant ensuring that the contributions of the very soft and soft components are the same at $p_T = p_{VS}$. Let us denote the rates of the very soft and soft components by k_{VS} and k_S, respectively. Then, $k_{VS} = \int_0^{p_{VS}} A_{VS} f_{VS}(p_T)dp_T$ and $k_S = \int_{p_{VS}}^{p_1} A_1 f_S(p_T)dp_T$, where $k_{VS} + k_S = k$ [for the definition of k, please refer to the section following Eq. (6)].

Although $f_{VS}(p_T)$ and $f_S(p_T)$ have the same form in Eq. (7), their contribution ranges are different. Similarly, the contribution range of $f_H(p_T)$ is different from those of $f_{VS}(p_T)$ and $f_S(p_T)$. The three functions have no correlation or dependence in the fitting procedure. We fitted $f_{VS}(p_T)$ at very soft p_T ranging from 0 to 0.5–1.5 GeV/c, $f_S(p_T)$ at soft p_T ranging from 0.5–1.5 to 2.5–3.5 GeV/c, and $f_H(p_T)$ at hard p_T ranging from 2.5–3.5 GeV/c to the maximum. In the case without $f_{VS}(p_T)$, Eq. (7) transforms into Eq. (6). Then, we fitted $f_S(p_T)$ in Eq. (6) in the range of 0 to 2.5–3.5 GeV/c. In the calculation, because of their different fractions, we used the weighted average of parameters in very soft and soft components in Eq. (7) to compare them with the values obtained from Eqs. (6) and (7).

3 Results and discussion

In Fig. 1, the transverse momentum spectra, $1/(2\pi p_T) \cdot d^2N/(dyd p_T)$, are shown for positively charged pions (π^+), positively charged kaons (K^+), and protons (p) (Fig. 1a, c), as well as for negatively charged pions (π^-), negatively charged kaons (K^-), and antiprotons ($\bar{p}$)(Fig. 1b, d) produced in (0–20% (Fig. 1a, b) and 60–88% (40–100%) (Fig. 1c, d) d–Au collisions at $\sqrt{s_{NN}} =$ 200 GeV. The closed and open symbols represent the experimental data of the PHENIX and STAR collaborations measured in the pseudorapidity range $|\eta| < 0.35$ [20] and the rapidity range $|y| < 0.5$ [21], respectively. The curves show the results obtained by models (i)–(iv), and the fitting parameters are given in Tables 1, 2, 3 and 4, respectively, with most of them are fitted by Eq. (6). The numerical values fitted by Eq. (7) are marked by a star at the end of the line, where the results obtained from the very soft and soft components are shown together. It can be seen that the four considered models describe the p_T spectra of the identified particles produced in central (0–20%) and peripheral (60–88% and 40–100%) d–Au collisions at $\sqrt{s_{NN}} = 200$ GeV similarly well.

Similarly, Figs. 1, 2a, b show the spectra of π^+, K^+, and p, as well as π^-, K^-, and $\bar{p}$, respectively, produced in pp collisions at $\sqrt{s} = 200$ GeV. The closed and open symbols represent the experimental data of the STAR collaboration measured in the range of $-0.5 < y < 0$ and at $|y| < 0.5$, respectively [22, 23]. The fitting parameters are given in Tables 1, 2, 3 and 4. It can be seen that the four considered models describe the p_T spectra of the identified particles produced in pp collisions at $\sqrt{s} = 200$ GeV similarly well.

Figure 3 is similar to Fig. 1, and it shows the spectra of $\pi^+ + \pi^-$, $K^+ + K^-$, and $p + \bar{p}$ produced in 0–5% (Fig. 3a) and 80–100% (Fig. 3b) p–Pb collisions at $\sqrt{s_{NN}} = 5.02$ TeV. The symbols represent the experimental data of the ALICE collaboration measured in the range of $-0.5 < y < 0$ [24]. It can be seen in most cases that the four considered models describe the p_T spectra of the identified particles produced in p–Pb collisions at $\sqrt{s_{NN}} = 5.02$ TeV similarly well.

Similarly, Fig. 4 shows the spectra, $(1/N_{EV}) \cdot 1/(2\pi p_T) \cdot d^2N/(dyd p_T)$, of $\pi^+ + \pi^-$, $K^+ + K^-$, and $p + \bar{p}$ produced in pp collisions at $\sqrt{s} = 2.76$ TeV, where N_{EV} denotes the number of events and it is typically omitted. The symbols represent the experimental data of

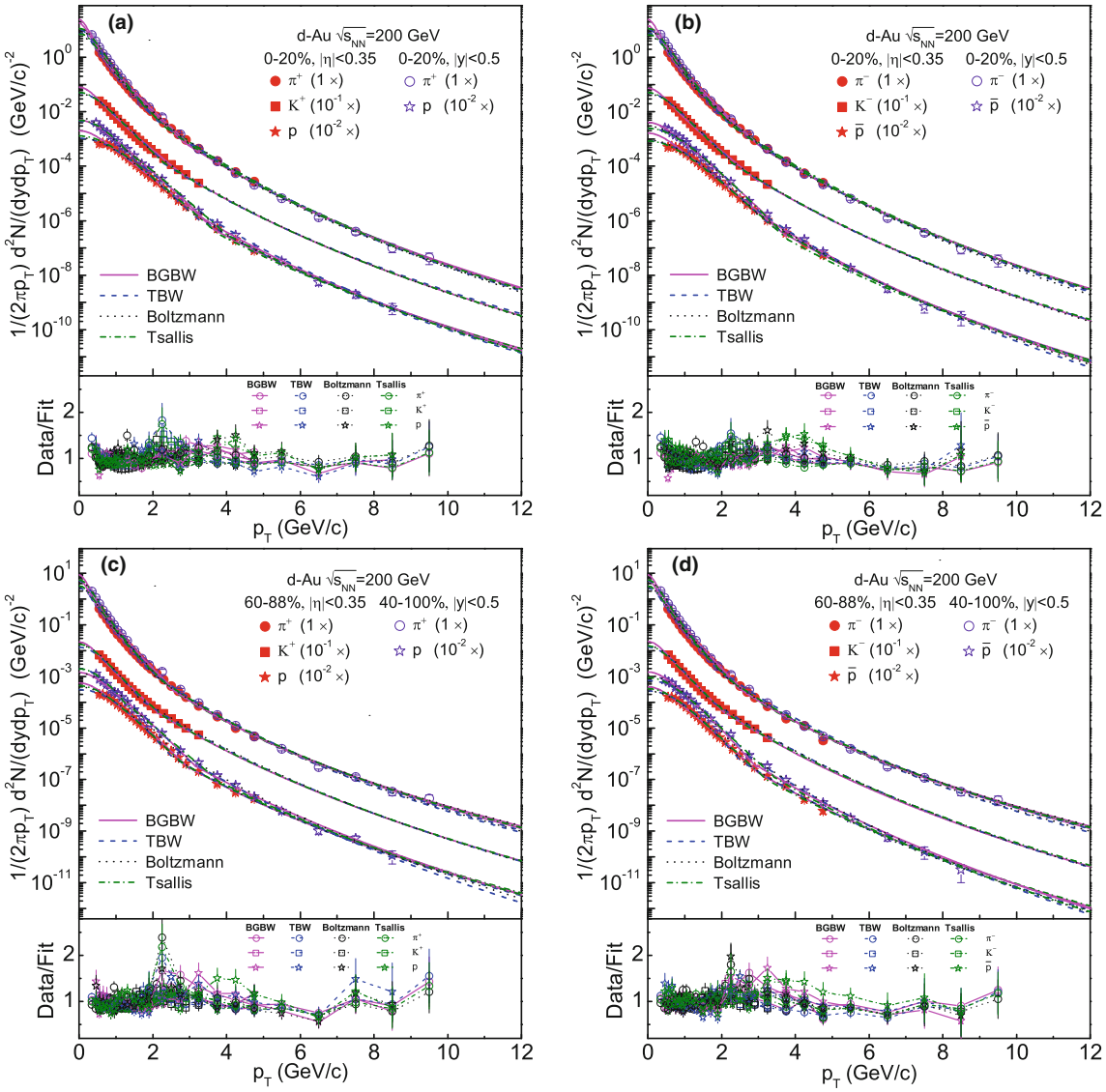

Fig. 1 (Color online) Transverse momentum spectra of π^+, K^+, and p (panels a and c), as well as π^-, K^-, and $\bar{p}$ (panels b and d) produced in 0–20% (panels a and b) and 60–88% (40–100%) (panels c and d) d–Au collisions at $\sqrt{s_{\rm NN}} = 200$ GeV. For clarity, the spectra for different particles are multiplied by different amounts shown in the panels. The closed and open symbols represent the experimental data of the PHENIX and STAR collaborations measured in $|\eta| < 0.35$ [20] and $|y| < 0.5$ [21], respectively. The solid, dashed, dotted, and dashed–dotted curves are our results fitted by Eqs. (6) and (7) in which $f_{\rm S}(p_{\rm T})$ ($f_{\rm VS}(p_{\rm T})$) denote $f_1(p_{\rm T})$, $f_2(p_{\rm T})$, $f_3(p_{\rm T})$, and $f_4(p_{\rm T})$, respectively. The bottom panels show the data for the fitting of the ratios

the ALICE collaboration measured in $|y| < 0.5$ for low-$p_{\rm T}$ particles and in $|\eta| < 0.8$ for high-$p_{\rm T}$ particles [25]. The four considered models describe the $p_{\rm T}$ spectra of the identified particles produced in pp collisions at $\sqrt{s} = 2.76$ TeV similarly well in most of the cases.

It should be noted that although we have used several free parameters in each fit, these parameters are restricted and irrelevant. A small number of them (1–3 parameters) are sensitive to the very soft component, which describes the very low $p_{\rm T}$ range from 0 to 0.5–1.5 GeV/c in certain cases. The same number of parameters (1–3) is sensitive to the soft component describing the low $p_{\rm T}$ range from 0.5–1.5 to 2.5–3.5 GeV/c in certain cases or typically in the range from 0 to 2.5–3.5 GeV/c. While the final two parameters (p_0 and n) are sensitive to the hard component describing the wide $p_{\rm T}$ range from 2.5–3.5 GeV/c to the maximum. In certain cases, the data in the very low $p_{\rm T}$ range is not available. In these cases, the number of free parameters is reduced by 1–3, and the low $p_{\rm T}$ range from 0 to 2.5–3.5 GeV/c can be used.

The last two models use the relations between T and m_0, $\langle p_{\rm T}\rangle$ and $\overline{m}$, as well as $\langle p\rangle$ and $\overline{m}$. Due to the mass dependences of the relations, these are not suitable to fit all particles simultaneously in the low $p_{\rm T}$ range. In principle,

Table 1 Values of parameters (T_0, β_T, k, p_0, and n), normalization constant (N_0), χ^2, and degrees of freedom (DOF) corresponding to the fits of the BGBW model and the inverse power law [Eqs. (1) and (5) through Eq. (6) or (7)] in Figs. 1, 2, 3, 4 and 8. For better readability, the collision types, data sources, and collision energies are listed in the blank spaces of the first two columns

Figure	Centrality	Particle	T_0 (GeV)	β_T (c)	k	p_0 (GeV/c)	n	N_0	χ^2/DOF
1(a)	0–20%	π^+	0.112 ± 0.006	0.43 ± 0.01	0.999 ± 0.001	5.0 ± 0.3	15.9 ± 0.4	4.85 ± 0.51	37/18
d–Au	200 GeV	K^+	0.128 ± 0.008	0.42 ± 0.01	0.994 ± 0.006	5.8 ± 0.3	16.5 ± 0.4	0.64 ± 0.07	9/15
PHENIX		p	0.130 ± 0.008	0.39 ± 0.01	0.998 ± 0.002	5.2 ± 0.3	15.2 ± 0.4	0.30 ± 0.02	64/18
1(b)	0–20%	π^-	0.121 ± 0.006	0.43 ± 0.01	0.999 ± 0.001	5.4 ± 0.3	16.7 ± 0.4	4.30 ± 0.50	23/18
		K^-	0.121 ± 0.008	0.43 ± 0.01	0.995 ± 0.004	6.1 ± 0.3	17.3 ± 0.4	0.60 ± 0.06	7/15
		$\bar{p}$	0.129 ± 0.008	0.39 ± 0.01	0.999 ± 0.001	5.1 ± 0.2	16.1 ± 0.4	0.24 ± 0.02	103/18
1(c)	60–88%	π^+	0.104 ± 0.006	0.43 ± 0.01	0.998 ± 0.002	3.5 ± 0.2	12.9 ± 0.3	1.29 ± 0.14	30/18
		K^+	0.116 ± 0.008	0.41 ± 0.01	0.982 ± 0.008	6.4 ± 0.2	17.2 ± 0.4	0.15 ± 0.02	12/15
		p	0.119 ± 0.009	0.37 ± 0.01	0.996 ± 0.004	5.5 ± 0.2	15.6 ± 0.3	0.07 ± 0.01	33/18
1(d)	60–88%	π^-	0.104 ± 0.006	0.43 ± 0.01	0.998 ± 0.002	3.5 ± 0.2	12.9 ± 0.3	1.29 ± 0.08	36/18
		K^-	0.115 ± 0.008	0.40 ± 0.01	0.983 ± 0.011	6.0 ± 0.2	17.2 ± 0.3	0.15 ± 0.02	15/15
		$\bar{p}$	0.119 ± 0.008	0.37 ± 0.01	0.997 ± 0.003	5.5 ± 0.2	16.6 ± 0.3	0.05 ± 0.01	31/18
1(a)	0–20%	π^+	0.111 ± 0.006	0.43 ± 0.01	0.999 ± 0.001	4.4 ± 0.2	15.3 ± 0.3	9.20 ± 0.99	21/18
d–Au	200 GeV	p	0.128 ± 0.008	0.37 ± 0.01	0.998 ± 0.002	5.1 ± 0.2	15.9 ± 0.3	0.97 ± 0.10	18/16
1(b)	0–20%	π^-	0.111 ± 0.006	0.43 ± 0.01	0.999 ± 0.001	4.4 ± 0.2	15.3 ± 0.3	9.2 ± 1.00	24/18
STAR		$\bar{p}$	0.127 ± 0.005	0.37 ± 0.01	0.998 ± 0.002	5.1 ± 0.1	16.9 ± 0.2	0.79 ± 0.09	21/16
1(c)	40–100%	π^+	0.103 ± 0.006	0.42 ± 0.01	0.999 ± 0.001	3.7 ± 0.2	13.4 ± 0.3	2.78 ± 0.28	26/18
		p	0.115 ± 0.007	0.37 ± 0.01	0.998 ± 0.002	6.9 ± 0.1	18.2 ± 0.3	0.25 ± 0.03	33/16
1(d)	40–100%	π^-	0.103 ± 0.006	0.42 ± 0.01	0.999 ± 0.001	3.7 ± 0.2	13.4 ± 0.3	2.78 ± 0.28	22/18
		$\bar{p}$	0.112 ± 0.006	0.35 ± 0.01	0.998 ± 0.002	6.4 ± 0.1	18.9 ± 0.3	0.24 ± 0.02	39/16
2(a)		π^+	0.104 ± 0.006	0.40 ± 0.01	0.999 ± 0.001	2.2 ± 0.1	11.2 ± 0.3	0.64 ± 0.07	22/23
pp	200 GeV	K^+	0.114 ± 0.008	0.41 ± 0.01	0.999 ± 0.001	3.0 ± 0.1	12.4 ± 0.3	0.07 ± 0.01	8/18
STAR		p	0.116 ± 0.008	0.34 ± 0.01	0.999 ± 0.001	3.1 ± 0.2	12.6 ± 0.3	0.05 ± 0.01	29/22
2(b)		π^-	0.104 ± 0.006	0.40 ± 0.01	0.999 ± 0.001	2.2 ± 0.1	11.3 ± 0.3	0.64 ± 0.07	27/23
		K^-	0.114 ± 0.008	0.41 ± 0.01	0.999 ± 0.001	3.2 ± 0.1	13.5 ± 0.3	0.07 ± 0.01	4/18
		$\bar{p}$	0.116 ± 0.008	0.34 ± 0.01	0.998 ± 0.002	3.1 ± 0.2	13.7 ± 0.4	0.04 ± 0.01	46/22
3(a)	0–5%	$\pi^\pm$	0.136 ± 0.008	0.43 ± 0.01	0.999 ± 0.001	2.1 ± 0.1	7.6 ± 0.3	18.70 ± 1.99	320/49*
p–Pb	5.02 TeV	$K^\pm$	0.193 ± 0.009	0.43 ± 0.01	0.997 ± 0.003	2.7 ± 0.1	7.3 ± 0.3	2.84 ± 0.41	71/45
ALICE		$p+\bar{p}$	0.195 ± 0.009	0.42 ± 0.01	0.999 ± 0.001	3.5 ± 0.2	8.8 ± 0.3	1.10 ± 0.11	172/43
3(b)	80–100%	$\pi^\pm$	0.112 ± 0.008	0.43 ± 0.01	0.988 ± 0.006	1.3 ± 0.1	7.4 ± 0.3	1.91 ± 0.20	234/52
		$K^\pm$	0.139 ± 0.008	0.41 ± 0.01	0.990 ± 0.006	3.3 ± 0.1	8.9 ± 0.3	0.25 ± 0.02	119/45
		$p+\bar{p}$	0.156 ± 0.009	0.37 ± 0.01	0.993 ± 0.006	3.9 ± 0.1	10.1 ± 0.3	0.10 ± 0.01	225/43
4		$\pi^\pm$	0.111 ± 0.008	0.43 ± 0.01	0.994 ± 0.005	1.9 ± 0.1	8.1 ± 0.3	3.60 ± 0.35	382/57
pp	2.76 TeV	$K^\pm$	0.143 ± 0.008	0.42 ± 0.01	0.990 ± 0.005	2.9 ± 0.1	8.6 ± 0.3	0.45 ± 0.05	119/52
ALICE		$p+\bar{p}$	0.152 ± 0.009	0.36 ± 0.01	0.991 ± 0.005	2.6 ± 0.1	9.5 ± 0.3	0.19 ± 0.01	214/43
8(a)	0–20%	$\pi^\pm$	0.107 ± 0.006	0.41 ± 0.01	0.999 ± 0.001	4.4 ± 0.3	14.5 ± 0.4	103.61 ± 11.37	28/23
Cu–Cu	200 GeV	$K^\pm$	0.122 ± 0.011	0.41 ± 0.02	0.997 ± 0.003	6.1 ± 0.3	16.3 ± 0.4	12.52 ± 1.26	1/10
		$p+\bar{p}$	0.125 ± 0.008	0.38 ± 0.01	0.999 ± 0.001	5.2 ± 0.3	15.7 ± 0.4	7.85 ± 0.77	5/21
8(b)	40–94%	$\pi^\pm$	0.101 ± 0.005	0.43 ± 0.01	0.999 ± 0.001	4.3 ± 0.2	14.5 ± 0.3	8.29 ± 0.81	18/23
		$K^\pm$	0.111 ± 0.008	0.40 ± 0.01	0.996 ± 0.003	5.9 ± 0.2	16.9 ± 0.3	1.28 ± 0.11	1/10
		$p+\bar{p}$	0.114 ± 0.009	0.37 ± 0.01	0.996 ± 0.003	6.4 ± 0.2	19.9 ± 0.2	0.50 ± 0.05	15/21

The results of the very soft and soft components are listed together and marked by an asterisk at the end of the line

simultaneous fits of all particles can be performed by using the first two models. In the case of simultaneous fits, a larger χ^2 can be obtained due to the same set of parameters. Although we fit different particle spectra by different sets of parameters, the mean value of a given parameter can be obtained by weighting different yields of the considered

Table 2 Values of parameters (T_0, q, β_T, k, p_0, and n), normalization constant (N_0), χ^2, and DOF corresponding to the fits of the TBW model and the inverse power law [Eqs. (2) and (5) through Eq. (6) or (7)] in Figs. 1, 2, 3, 4, and 8, where the columns of centrality and particle are the same as those in Table 1; thus, these are omitted

Figure	T_0 (GeV)	q	β_T (c)	k	p_0 (GeV/c)	n	N_0	χ^2/DOF
1(a)	0.108 ± 0.006	1.025 ± 0.007	0.46 ± 0.01	0.991 ± 0.005	4.8 ± 0.3	16.2 ± 0.4	3.86 ± 0.39	46/17
d–Au	0.118 ± 0.008	1.026 ± 0.008	0.46 ± 0.01	0.981 ± 0.006	5.9 ± 0.3	16.0 ± 0.4	0.57 ± 0.06	24/14
PHENIX	0.119 ± 0.008	1.018 ± 0.007	0.45 ± 0.01	0.996 ± 0.004	5.1 ± 0.2	15.9 ± 0.4	0.25 ± 0.02	19/17
1(b)	0.108 ± 0.006	1.025 ± 0.007	0.46 ± 0.01	0.992 ± 0.005	4.8 ± 0.3	16.4 ± 0.4	3.86 ± 0.39	56/17
	0.118 ± 0.008	1.026 ± 0.008	0.46 ± 0.01	0.983 ± 0.009	5.9 ± 0.3	17.0 ± 0.4	0.57 ± 0.06	34/14
	0.118 ± 0.008	1.018 ± 0.007	0.45 ± 0.01	0.996 ± 0.004	5.1 ± 0.2	16.3 ± 0.4	0.20 ± 0.02	36/17
1(c)	0.088 ± 0.006	1.045 ± 0.008	0.46 ± 0.01	0.994 ± 0.004	3.5 ± 0.2	13.7 ± 0.3	1.02 ± 0.10	34/17
	0.090 ± 0.008	1.029 ± 0.008	0.46 ± 0.01	0.955 ± 0.011	6.4 ± 0.3	17.5 ± 0.4	0.13 ± 0.01	9/14
	0.098 ± 0.008	1.012 ± 0.007	0.44 ± 0.01	0.990 ± 0.006	5.5 ± 0.2	15.9 ± 0.2	0.06 ± 0.01	37/17
1(d)	0.088 ± 0.006	1.045 ± 0.008	0.46 ± 0.01	0.994 ± 0.006	3.5 ± 0.2	13.7 ± 0.3	1.02 ± 0.10	46/17
	0.090 ± 0.008	1.029 ± 0.008	0.46 ± 0.01	0.957 ± 0.011	6.7 ± 0.3	18.6 ± 0.4	0.13 ± 0.01	11/14
	0.097 ± 0.008	1.012 ± 0.007	0.43 ± 0.01	0.992 ± 0.006	5.5 ± 0.2	17.1 ± 0.3	0.05 ± 0.01	48/17
1(a)	0.106 ± 0.006	1.020 ± 0.008	0.46 ± 0.01	0.995 ± 0.004	4.4 ± 0.2	15.6 ± 0.4	7.07 ± 0.76	38/17
d–Au	0.115 ± 0.008	1.010 ± 0.007	0.38 ± 0.01	0.998 ± 0.002	4.4 ± 0.2	15.6 ± 0.4	0.96 ± 0.10	35/11*
1(b)	0.106 ± 0.006	1.020 ± 0.008	0.46 ± 0.01	0.995 ± 0.004	4.4 ± 0.2	15.6 ± 0.4	7.07 ± 0.76	39/17
STAR	0.116 ± 0.008	1.008 ± 0.005	0.44 ± 0.01	0.997 ± 0.003	5.1 ± 0.2	17.7 ± 0.4	0.73 ± 0.07	44/15
1(c)	0.085 ± 0.006	1.038 ± 0.008	0.46 ± 0.01	0.996 ± 0.004	3.7 ± 0.2	13.9 ± 0.3	2.50 ± 0.25	33/17
	0.090 ± 0.008	1.008 ± 0.007	0.35 ± 0.01	0.998 ± 0.002	6.9 ± 0.2	19.6 ± 0.4	0.31 ± 0.02	29/11*
1(d)	0.085 ± 0.006	1.038 ± 0.008	0.46 ± 0.01	0.996 ± 0.004	3.7 ± 0.2	13.9 ± 0.3	2.54 ± 0.25	48/17
	0.094 ± 0.008	1.016 ± 0.007	0.44 ± 0.01	0.996 ± 0.004	5.9 ± 0.2	19.4 ± 0.3	0.19 ± 0.02	53/15
2(a)	0.089 ± 0.006	1.023 ± 0.008	0.44 ± 0.01	0.997 ± 0.003	2.2 ± 0.1	11.2 ± 0.4	0.62 ± 0.06	41/22
pp	0.098 ± 0.008	1.029 ± 0.009	0.43 ± 0.01	0.996 ± 0.004	3.0 ± 0.2	12.8 ± 0.4	0.07 ± 0.01	29/17
STAR	0.104 ± 0.009	1.006 ± 0.001	0.39 ± 0.01	0.996 ± 0.004	3.1 ± 0.2	13.5 ± 0.4	0.05 ± 0.01	55/21
2(b)	0.089 ± 0.006	1.023 ± 0.008	0.44 ± 0.01	0.997 ± 0.003	2.2 ± 0.1	11.5 ± 0.4	0.62 ± 0.06	52/22
	0.098 ± 0.008	1.029 ± 0.009	0.43 ± 0.01	0.996 ± 0.004	3.0 ± 0.2	13.8 ± 0.4	0.07 ± 0.01	26/17
	0.104 ± 0.009	1.006 ± 0.001	0.39 ± 0.01	0.996 ± 0.004	3.1 ± 0.2	13.9 ± 0.4	0.04 ± 0.01	84/21
3(a)	0.107 ± 0.007	1.001 ± 0.001	0.48 ± 0.01	0.999 ± 0.001	2.2 ± 0.1	7.7 ± 0.3	20.98 ± 2.00	323/47*
p–Pb	0.188 ± 0.009	1.012 ± 0.006	0.48 ± 0.01	0.995 ± 0.004	2.7 ± 0.2	7.8 ± 0.3	2.78 ± 0.29	436/44
ALICE	0.198 ± 0.009	1.013 ± 0.008	0.47 ± 0.01	0.999 ± 0.001	3.5 ± 0.2	9.1 ± 0.3	1.10 ± 0.10	223/42
3(b)	0.089 ± 0.006	1.001 ± 0.001	0.45 ± 0.01	0.999 ± 0.001	1.4 ± 0.1	7.3 ± 0.3	2.21 ± 0.20	606/43*
	0.113 ± 0.008	1.023 ± 0.006	0.45 ± 0.01	0.976 ± 0.010	3.3 ± 0.2	9.1 ± 0.3	0.23 ± 0.02	325/44
	0.115 ± 0.009	1.002 ± 0.001	0.45 ± 0.01	0.982 ± 0.010	3.9 ± 0.2	10.6 ± 0.3	0.09 ± 0.01	493/42
4	0.089 ± 0.006	1.001 ± 0.001	0.45 ± 0.01	0.999 ± 0.001	1.7 ± 0.1	7.8 ± 0.3	4.00 ± 0.31	485/48*
pp	0.113 ± 0.008	1.013 ± 0.006	0.48 ± 0.01	0.975 ± 0.010	2.9 ± 0.1	9.0 ± 0.3	0.46 ± 0.05	376/51
ALICE	0.116 ± 0.008	1.004 ± 0.001	0.44 ± 0.01	0.975 ± 0.010	2.5 ± 0.2	9.9 ± 0.3	0.20 ± 0.02	494/42
8(a)	0.101 ± 0.007	1.027 ± 0.009	0.47 ± 0.02	0.999 ± 0.001	4.4 ± 0.2	14.8 ± 0.4	66.17 ± 7.10	27/22
Cu–Cu	0.110 ± 0.008	1.026 ± 0.008	0.46 ± 0.02	0.996 ± 0.004	6.2 ± 0.3	16.5 ± 0.4	12.23 ± 1.20	3/9
	0.114 ± 0.008	1.020 ± 0.007	0.45 ± 0.01	0.999 ± 0.001	5.2 ± 0.3	16.3 ± 0.4	6.02 ± 0.60	4/20
8(b)	0.085 ± 0.007	1.052 ± 0.008	0.47 ± 0.02	0.999 ± 0.001	4.3 ± 0.2	14.7 ± 0.3	6.58 ± 0.68	19/22
	0.090 ± 0.008	1.029 ± 0.008	0.47 ± 0.02	0.996 ± 0.004	6.0 ± 0.3	16.7 ± 0.3	1.08 ± 0.01	3/9
	0.095 ± 0.008	1.012 ± 0.008	0.46 ± 0.01	0.992 ± 0.004	6.6 ± 0.2	21.3 ± 0.4	0.38 ± 0.04	12/20

particles. Thus, the weighted mean parameter can be regarded as a parameter suitable for the simultaneous fit of all particles. Therefore, both the simultaneous and non-simultaneous fits can be used in the analysis of the particle spectra.

Based on the descriptions of the p_T spectra, the first two models can conveniently provide T_0 and β_T; however, the

Table 3 Values of parameters (T, k, p_0, and n), normalization constant (N_0), χ^2, and DOF corresponding to the fits of the Boltzmann distribution and the inverse power law [Eqs. (3) and (5) through Eq. (6) or (7)] in Figs. 1, 2, 3, 4, and 8

Figure	Centrality	Particle	T (GeV)	k	p_0 (GeV/c)	n	N_0	χ^2/DOF
1(a)	0–20%	π^+	0.179 ± 0.006	0.992 ± 0.005	4.9 ± 0.2	16.8 ± 0.3	3.70 ± 0.35	28/17*
d–Au	200 GeV	K^+	0.243 ± 0.009	0.976 ± 0.011	5.9 ± 0.2	16.9 ± 0.3	0.60 ± 0.05	39/16
PHENIX		p	0.293 ± 0.009	0.991 ± 0.006	5.1 ± 0.2	15.8 ± 0.3	0.25 ± 0.02	24/19
1(b)	0–20%	π^-	0.179 ± 0.006	0.993 ± 0.006	4.8 ± 0.2	16.8 ± 0.3	3.70 ± 0.35	29/17*
		K^-	0.240 ± 0.009	0.974 ± 0.011	5.6 ± 0.2	16.9 ± 0.3	0.58 ± 0.05	37/16
		$\bar{p}$	0.290 ± 0.009	0.993 ± 0.005	5.0 ± 0.2	16.5 ± 0.3	0.20 ± 0.02	30/19
1(c)	60–88%	π^+	0.148 ± 0.006	0.995 ± 0.005	3.5 ± 0.1	13.5 ± 0.2	1.14 ± 0.01	61/17*
		K^+	0.200 ± 0.009	0.950 ± 0.011	6.4 ± 0.3	17.7 ± 0.3	0.15 ± 0.01	18/16
		p	0.247 ± 0.009	0.993 ± 0.005	5.3 ± 0.2	15.5 ± 0.3	0.07 ± 0.01	42/19
1(d)	60–88%	π^-	0.148 ± 0.006	0.995 ± 0.004	3.5 ± 0.1	13.5 ± 0.2	1.14 ± 0.01	70/17*
		K^-	0.200 ± 0.009	0.954 ± 0.012	6.2 ± 0.3	17.9 ± 0.3	0.14 ± 0.01	17/16
		$\bar{p}$	0.247 ± 0.009	0.993 ± 0.005	5.0 ± 0.2	16.5 ± 0.3	0.05 ± 0.01	28/19
1(a)	0–20%	π^+	0.172 ± 0.007	0.999 ± 0.001	4.1 ± 0.1	15.0 ± 0.3	7.70 ± 0.70	42/17*
d–Au	200 GeV	p	0.208 ± 0.009	0.999 ± 0.001	5.8 ± 0.2	16.5 ± 0.3	1.07 ± 0.10	28/15*
1(b)	0–20%	π^-	0.172 ± 0.007	0.999 ± 0.001	4.1 ± 0.1	15.0 ± 0.3	7.70 ± 0.70	36/17*
STAR		$\bar{p}$	0.253 ± 0.008	0.997 ± 0.003	5.2 ± 0.2	17.2 ± 0.3	0.73 ± 0.06	33/17
1(c)	40–100%	π^+	0.143 ± 0.007	0.998 ± 0.002	3.1 ± 0.1	12.4 ± 0.2	2.63 ± 0.24	59/17*
		p	0.219 ± 0.009	0.991 ± 0.005	5.8 ± 0.2	17.8 ± 0.3	0.27 ± 0.02	37/17
1(d)	40–100%	π^-	0.143 ± 0.007	0.998 ± 0.002	3.1 ± 0.1	12.4 ± 0.2	2.63 ± 0.24	49/17*
		$\bar{p}$	0.217 ± 0.009	0.992 ± 0.005	5.4 ± 0.1	18.5 ± 0.3	0.22 ± 0.02	30/17
2(a)		π^+	0.144 ± 0.007	0.999 ± 0.001	2.0 ± 0.1	10.8 ± 0.3	0.55 ± 0.33	35/22*
pp	200 GeV	K^+	0.203 ± 0.009	0.989 ± 0.007	3.3 ± 0.1	13.3 ± 0.3	0.07 ± 0.01	31/19
STAR		p	0.234 ± 0.009	0.997 ± 0.003	3.2 ± 0.2	13.6 ± 0.3	0.05 ± 0.01	121/23
2(b)		π^-	0.144 ± 0.007	0.999 ± 0.001	2.0 ± 0.1	10.8 ± 0.3	0.55 ± 0.33	47/22*
		K^-	0.203 ± 0.009	0.991 ± 0.005	3.1 ± 0.1	13.7 ± 0.3	0.07 ± 0.01	21/19
		$\bar{p}$	0.230 ± 0.009	0.996 ± 0.004	3.1 ± 0.2	14.3 ± 0.3	0.04 ± 0.01	91/23
3(a)	0–5%	$\pi^\pm$	0.163 ± 0.008	0.999 ± 0.001	2.0 ± 0.1	7.7 ± 0.3	22.14 ± 2.10	852/49*
p–Pb	5.02 TeV	$K^\pm$	0.297 ± 0.008	0.992 ± 0.005	3.4 ± 0.1	8.6 ± 0.3	2.87 ± 0.29	110/44*
ALICE		$p+\bar{p}$	0.381 ± 0.009	0.997 ± 0.003	3.2 ± 0.1	9.4 ± 0.3	1.17 ± 0.01	138/42*
3(b)	80–100%	$\pi^\pm$	0.123 ± 0.009	0.999 ± 0.001	1.4 ± 0.1	7.2 ± 0.3	2.23 ± 0.19	935/49*
		$K^\pm$	0.212 ± 0.010	0.995 ± 0.005	3.8 ± 0.1	9.0 ± 0.3	0.28 ± 0.02	403/44*
		$p+\bar{p}$	0.235 ± 0.010	0.997 ± 0.003	3.3 ± 0.1	9.8 ± 0.3	0.11 ± 0.01	128/42*
4		$\pi^\pm$	0.123 ± 0.008	0.997 ± 0.003	1.7 ± 0.1	7.9 ± 0.3	4.14 ± 0.31	688/54*
pp	2.76 TeV	$K^\pm$	0.205 ± 0.009	0.988 ± 0.010	2.8 ± 0.1	8.7 ± 0.3	0.49 ± 0.06	178/51*
ALICE		$p+\bar{p}$	0.241 ± 0.009	0.995 ± 0.005	2.6 ± 0.1	9.5 ± 0.3	0.20 ± 0.02	104/42*
8(a)	0–20%	$\pi^\pm$	0.179 ± 0.008	0.999 ± 0.001	4.2 ± 0.1	14.5 ± 0.2	72.07 ± 7.00	35/22*
Cu–Cu	200 GeV	$K^\pm$	0.231 ± 0.010	0.991 ± 0.006	5.9 ± 0.2	16.9 ± 0.3	12.37 ± 1.21	5/11
		$p+\bar{p}$	0.296 ± 0.009	0.999 ± 0.001	5.4 ± 0.2	17.0 ± 0.4	5.81 ± 0.67	6/22
8(b)	40–94%	$\pi^\pm$	0.139 ± 0.006	0.999 ± 0.001	3.8 ± 0.1	13.9 ± 0.2	10.95 ± 0.89	23/22*
		$K^\pm$	0.179 ± 0.009	0.994 ± 0.005	4.9 ± 0.1	16.2 ± 0.3	1.16 ± 0.13	1/9*
		$p+\bar{p}$	0.245 ± 0.008	0.999 ± 0.001	4.8 ± 0.2	17.7 ± 0.3	0.43 ± 0.06	3/20*

values of parameters are possibly not the same according to different models. To obtain the values of T_0, β_T, and β by models (iii) and (iv), we analyze the values of T presented in Tables 3 and 4, and calculate $\langle p_T \rangle$, $\langle p \rangle$, and $\overline{m}$ based on these values. That is, we derived $\langle p_T \rangle$, $\langle p \rangle$, and $\overline{m}$ by using a more complex fitting of Boltzmann and Tsallis distributions in the p_T range from 0 to p_1; however, as the data was unavailable in certain regions, the

Table 4 Values of parameters (T, q, k, p_0, and n), normalization constant (N_0), χ^2, and DOF corresponding to the fits of the Tsallis distribution and the inverse power law [Eqs. (4) and (5) through Eq. (6) or (7)] in Figs. 1, 2, 3, 4, and 8

Figure	Centrality	Particle	T (GeV)	q	k	p_0 (GeV/c)	n	N_0	χ^2/DOF
1(a)	0–20%	π^+	0.134 ± 0.008	1.082 ± 0.009	0.994 ± 0.005	4.8 ± 0.2	16.3 ± 0.4	3.93 ± 0.36	32/18
d–Au	200 GeV	K^+	0.189 ± 0.009	1.052 ± 0.010	0.980 ± 0.010	6.1 ± 0.2	16.9 ± 0.4	0.57 ± 0.06	13/15
PHENIX		p	0.272 ± 0.009	1.015 ± 0.007	0.999 ± 0.001	5.5 ± 0.2	15.3 ± 0.4	0.28 ± 0.02	49/18
1(b)	0–20%	π^-	0.134 ± 0.008	1.082 ± 0.009	0.993 ± 0.005	4.8 ± 0.2	16.8 ± 0.4	3.68 ± 0.36	33/18
		K^-	0.189 ± 0.009	1.052 ± 0.010	0.982 ± 0.011	6.0 ± 0.2	17.1 ± 0.4	0.56 ± 0.06	18/15
		$\bar{p}$	0.273 ± 0.009	1.015 ± 0.007	0.999 ± 0.001	5.4 ± 0.2	16.0 ± 0.4	0.18 ± 0.02	44/18
1(c)	y60–88%	π^+	0.108 ± 0.008	1.099 ± 0.009	0.999 ± 0.001	3.6 ± 0.1	13.1 ± 0.3	1.20 ± 0.12	37/18
		K^+	0.141 ± 0.009	1.083 ± 0.011	0.984 ± 0.012	6.6 ± 0.2	17.5 ± 0.4	0.15 ± 0.02	16/15
		p	0.194 ± 0.010	1.035 ± 0.010	0.996 ± 0.004	5.8 ± 0.2	15.9 ± 0.4	0.07 ± 0.01	22/18
1(d)	60–88%	π^-	0.108 ± 0.008	1.099 ± 0.009	0.999 ± 0.001	3.5 ± 0.1	12.9 ± 0.3	1.17 ± 0.12	36/18
		K^-	0.141 ± 0.009	1.083 ± 0.011	0.979 ± 0.012	6.5 ± 0.2	17.8 ± 0.4	0.13 ± 0.02	11/15
		$\bar{p}$	0.194 ± 0.010	1.035 ± 0.010	0.998 ± 0.002	5.8 ± 0.2	16.6 ± 0.4	0.05 ± 0.01	30/18
1(a)	0–20%	π^+	0.129 ± 0.008	1.076 ± 0.009	0.997 ± 0.003	4.4 ± 0.1	15.4 ± 0.4	8.03 ± 0.80	26/18
d–Au	200 GeV	p	0.221 ± 0.009	1.005 ± 0.005	0.999 ± 0.001	5.9 ± 0.2	16.8 ± 0.3	1.01 ± 0.09	23/13*
1(b)	0–20%	π^-	0.129 ± 0.008	1.076 ± 0.009	0.997 ± 0.003	4.4 ± 0.1	15.4 ± 0.4	8.03 ± 0.80	27/18
STAR		$\bar{p}$	0.260 ± 0.009	1.009 ± 0.005	0.999 ± 0.001	5.7 ± 0.2	17.3 ± 0.3	0.68 ± 0.07	46/16
1(c)	40–100%	π^+	0.104 ± 0.008	1.089 ± 0.009	0.998 ± 0.002	3.4 ± 0.1	13.1 ± 0.3	2.62 ± 0.25	32/18
		p	0.173 ± 0.009	1.011 ± 0.005	0.999 ± 0.001	6.3 ± 0.2	17.0 ± 0.3	0.31 ± 0.03	33/13*
1(d)	40–100%	π^-	0.104 ± 0.008	1.089 ± 0.009	0.998 ± 0.002	3.4 ± 0.1	13.1 ± 0.3	2.62 ± 0.25	26/18
		$\bar{p}$	0.189 ± 0.009	1.036 ± 0.005	0.999 ± 0.001	5.4 ± 0.2	17.7 ± 0.3	0.19 ± 0.02	35/16
2(a)		π^+	0.120 ± 0.008	1.051 ± 0.009	0.997 ± 0.003	2.1 ± 0.1	10.9 ± 0.3	0.60 ± 0.05	44/23
pp	200 GeV	K^+	0.153 ± 0.009	1.057 ± 0.011	0.997 ± 0.003	3.5 ± 0.1	13.2 ± 0.3	0.07 ± 0.01	14/18
STAR		p	0.190 ± 0.009	1.019 ± 0.009	0.997 ± 0.003	3.3 ± 0.1	13.3 ± 0.4	0.05 ± 0.01	32/22
2(b)		π^-	0.120 ± 0.008	1.056 ± 0.009	0.997 ± 0.003	2.1 ± 0.1	11.0 ± 0.3	0.56 ± 0.05	45/23
		K^-	0.153 ± 0.009	1.057 ± 0.011	0.998 ± 0.002	3.5 ± 0.1	13.9 ± 0.3	0.07 ± 0.01	7/18
		$\bar{p}$	0.190 ± 0.009	1.019 ± 0.009	0.997 ± 0.003	3.3 ± 0.1	13.9 ± 0.4	0.04 ± 0.01	42/22
3(a)	0–5%	$\pi^\pm$	0.156 ± 0.008	1.031 ± 0.012	0.999 ± 0.001	2.2 ± 0.1	7.7 ± 0.3	21.20 ± 1.91	934/45*
p–Pb	5.02 TeV	$K^\pm$	0.262 ± 0.008	1.059 ± 0.011	0.995 ± 0.005	3.0 ± 0.1	7.8 ± 0.3	2.78 ± 0.28	261/45
ALICE		$p+\bar{p}$	0.351 ± 0.009	1.035 ± 0.009	0.999 ± 0.001	3.4 ± 0.1	9.1 ± 0.3	1.09 ± 0.01	97/43
3(b)	80–100%	$\pi^\pm$	0.111 ± 0.008	1.042 ± 0.009	0.998 ± 0.002	1.4 ± 0.1	7.3 ± 0.3	2.15 ± 0.20	389/49*
		$K^\pm$	0.171 ± 0.008	1.068 ± 0.012	0.986 ± 0.010	3.8 ± 0.1	9.3 ± 0.3	0.23 ± 0.02	282/45
		$p+\bar{p}$	0.192 ± 0.009	1.056 ± 0.011	0.993 ± 0.005	3.4 ± 0.1	9.8 ± 0.3	0.10 ± 0.01	230/43
4		$\pi^\pm$	0.112 ± 0.008	1.042 ± 0.004	0.997 ± 0.003	1.7 ± 0.1	7.9 ± 0.3	3.90 ± 0.36	461/54*
pp	2.76 TeV	$K^\pm$	0.175 ± 0.009	1.071 ± 0.011	0.985 ± 0.010	2.8 ± 0.1	8.7 ± 0.3	0.44 ± 0.06	253/52
ALICE		$p+\bar{p}$	0.223 ± 0.009	1.029 ± 0.008	0.988 ± 0.010	2.6 ± 0.1	9.5 ± 0.3	0.19 ± 0.02	373/43
8(a)	0–20%	π^+	0.131 ± 0.007	1.070 ± 0.006	0.999 ± 0.001	4.4 ± 0.2	14.6 ± 0.3	73.32 ± 8.01	23/23
Cu–Cu	200 GeV	K^+	0.173 ± 0.011	1.055 ± 0.010	0.997 ± 0.003	6.4 ± 0.2	16.9 ± 0.4	12.42 ± 1.31	1/10
		p	0.250 ± 0.009	1.018 ± 0.006	0.995 ± 0.005	5.4 ± 0.2	16.4 ± 0.3	6.30 ± 0.75	6/21
8(b)	40–94%	π^+	0.105 ± 0.006	1.096 ± 0.006	0.999 ± 0.001	4.4 ± 0.3	14.1 ± 0.4	7.90 ± 0.83	23/23
		K^+	0.139 ± 0.009	1.076 ± 0.009	0.998 ± 0.002	5.2 ± 0.3	15.9 ± 0.4	1.08 ± 0.12	1/10
		p	0.197 ± 0.009	1.042 ± 0.006	0.995 ± 0.005	5.1 ± 0.2	17.9 ± 0.3	0.43 ± 0.04	9/21

simple counting of published spectra could not be used. Based on an isotropic assumption in the rest frame of the emission source and using a Monte Carlo method, we can perform the calculations according to p_T to obtain $\langle p \rangle$ and $\overline{m}$ [15–17]. It can seen that there are other constraints in the statistical fits due to the excluding contribution of the hard component and the selecting reference frame of the emission source.

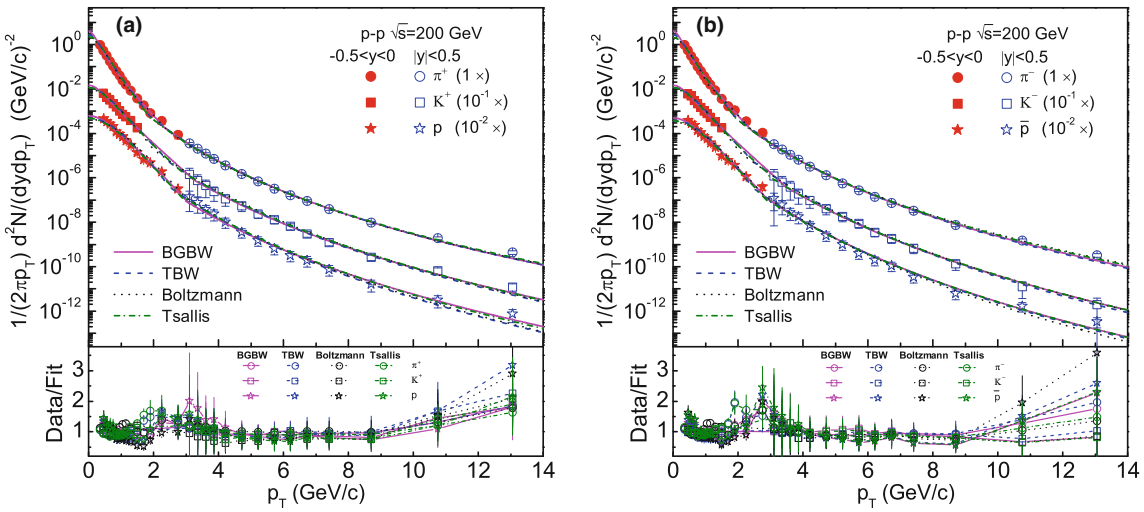

Fig. 2 (Color online) Spectra of π^+, K^+, and p (panel a), as well as π^-, K^-, and $\bar{p}$ (panel b), produced in pp collisions at $\sqrt{s} = 200$ GeV. The closed and open symbols represent the experimental data of the STAR collaboration measured in $-0.5 < y < 0$ and $|y| < 0.5$, respectively [22, 23]

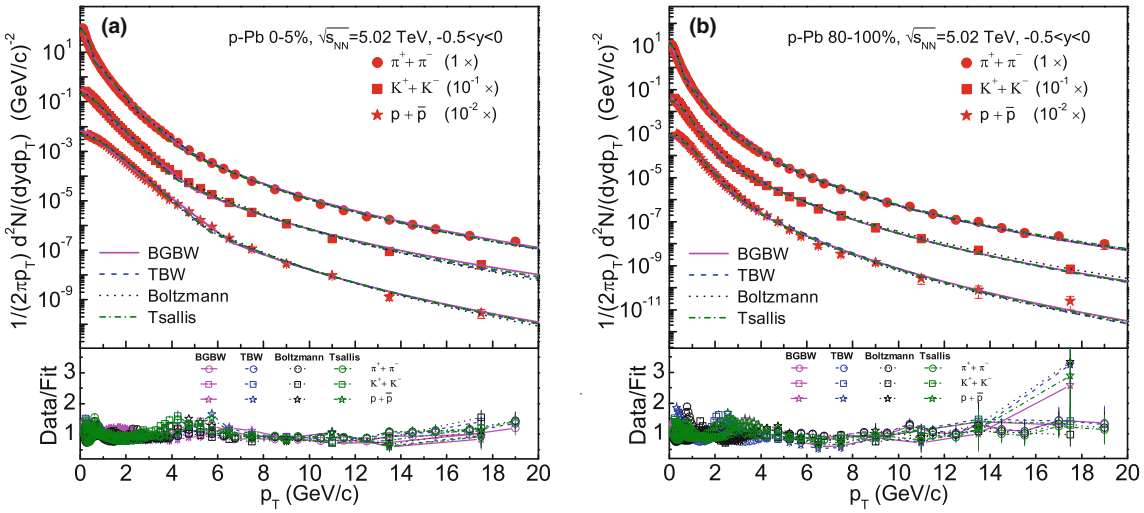

Fig. 3 (Color online) Spectra of $\pi^+ + \pi^-$, $K^+ + K^-$, and $p + \bar{p}$ produced in 0–5% (panel a) and 80–100% (panel b) p–Pb collisions at $\sqrt{s_{\rm NN}} = 5.02$ TeV. The symbols represent the experimental data of the ALICE collaboration measured in the range of $-0.5 < y < 0$ [24]

The relations between T and m_0, $\langle p_{\rm T} \rangle$ and $\overline{m}$, as well as $\langle p \rangle$ and $\overline{m}$ are shown in Figs. 5, 6 and 7, respectively, where panels a and b correspond to models (iii) and (iv) using Boltzmann and Tsallis distributions, respectively. The symbols in Fig. 5 represent values of T listed in Tables 3 and 4 for different m_0 values. The symbols in Figs. 6 and 7 represent values of $\langle p_{\rm T} \rangle$ and $\langle p \rangle$ for different $\overline{m}$ values, respectively, which are calculated from the parameters listed in Tables 3 and 4 and by an isotropic assumption in the rest frame of the emission source. The error bars in the three figures represent overall errors. Although the method of least squares was used to provide an appropriate connection, the lines in the three figures connect the points for a better visibility in each event sample. The intercept in Fig. 5 provides T_0, and $\beta_{\rm T}$ and β can be obtained from the slopes in Figs. 6 and 7, respectively. The values of T, T_0, $\beta_{\rm T}$, β, and $\overline{m}$ can be considered independent of isospin.

To compare values of key parameters obtained by different models for different event samples, in the following we discuss the qualitative dependences of T_0 and $\beta_{\rm T}$ on the centrality. From Tables 1 and 2, we can obtain T_0 and $\beta_{\rm T}$ in the first two models by weighting the yields of different particles. From the intercept in Fig. 5, T_0 can be obtained in the last two models, while from the slope in Fig. 6 (or 7), we can obtain $\beta_{\rm T}$ (or β) in the last two models. Generally, the four models present similar results, and in certain cases these results are in agreement with each other within errors. In central d–Au and p–Pb collisions, T_0 is relatively greater than that in peripheral collisions. Ranging

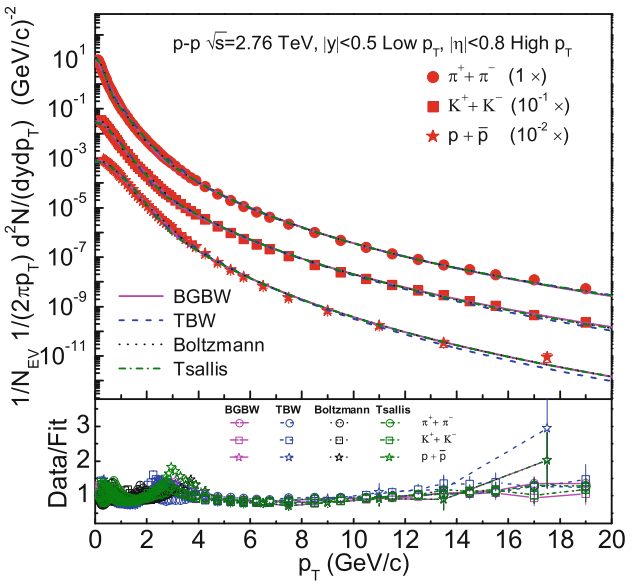

Fig. 4 (Color online) Spectra of $\pi^+ + \pi^-$, $K^+ + K^-$, and $p + \bar{p}$ produced in pp collisions at $\sqrt{s} = 2.76$ TeV. The symbols represent the experimental data of the ALICE collaboration measured in $|y| < 0.5$ for low-p_T particles and in $|\eta| < 0.8$ for high-p_T particles [25]

from the RHIC to LHC energies, T_0 shows a slight increase or it is nearly invariant. Ranging from the peripheral to central collisions and from the RHIC to LHC energies, both β_T values show a slight increase or they are nearly invariant. These conditions are in agreement with our recent work, which studied Au–Au collisions at the RHIC and Pb–Pb collisions at the LHC [14] by a slightly different superposition. In particular, the absolute values of T_0 and β_T do not show obvious change in the range from d–Au (p–Pb) to Au–Au (Pb–Pb) collisions, except for a systematical increase ($\leq 5\%$) due to different superpositions. In pp collisions, the dependences of T_0 and β_T on $\sqrt{s}$ are similar to those in peripheral nuclear (d–Au, Au–Au, p–Pb, and Pb–Pb) collisions.

Apparently, in the above discussions T_0 and β_T are related to the physical properties of an expanding thermal system, which, in the present work, is a high-energy collision system with a given impact parameter. If a mini-bias data sample is considered, T_0 and β_T are the averages over various impact parameters. In particular, T_0 and β_T in central (peripheral) collisions are the averages over a given centrality range. For pp collisions without choosing a centrality, T_0 and β_T are the averages over a given data sample and they are related to the physical properties of the sample. In terms of excitation degree, characterized by T_0, nuclear collisions, such as d–Au and Au–Au collisions at the RHIC and p–Pb and Pb–Pb collisions at the LHC, show similar excitation degree at the kinetic freeze-out; however, the excitation degree in central collisions is slightly higher than that in peripheral collisions. The excitation degree depends on the heaviest nucleus, but independent of the total nucleus, minimum nucleus, numbers of participating nucleons, and binary collisions in nuclear collisions at a given energy.

To confirm the above statement of the heaviest nucleus, instead of using the total nucleus to determine T_0, in the following we analyze copper–copper (Cu–Cu) collisions. Figure 8 shows the spectra of $\pi^+ + \pi^-$, $K^+ + K^-$, and $p + \bar{p}$ produced in 0–20% (Fig. 8a) and 40–94% (60–92%, 60–94%, and 40–60%) (Fig. 8b) Cu–Cu collisions at $\sqrt{s_{NN}} = 200$ GeV. The closed and open symbols represent the experimental data of the PHENIX and STAR collaborations measured in $|\eta| < 0.35$ and $|y| < 0.5$, respectively [29, 30], where the data of the 0–20% collisions is obtained by combining different centralities (0–5%, 5–10%, and 10–20%) to match with those in Fig. 1, and the data measured

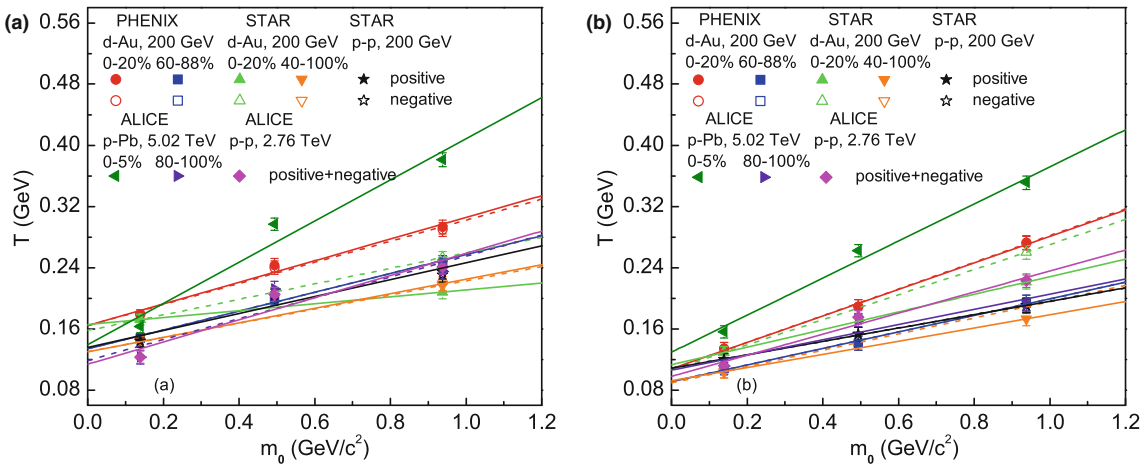

Fig. 5 (Color online) Relationship of T and m_0, where panels a and b correspond to models (iii) and (iv) using Boltzmann and Tsallis distributions, respectively. The symbols represent values of T listed in Tables 3 and 4 for different m_0 values. The lines connect the points for better visibility

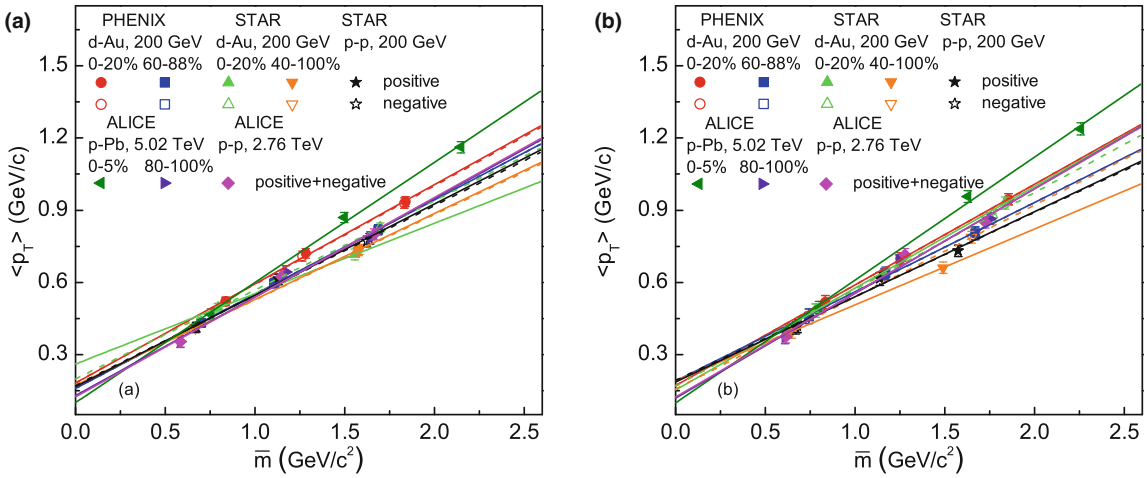

Fig. 6 (Color online) Relationship of $\langle p_T \rangle$ and $\overline{m}$. The symbols represent values of $\langle p_T \rangle$ for different $\overline{m}$ values, calculated from the parameters listed in Tables 3 and 4 and by an isotropic assumption in the rest frame of the emission source

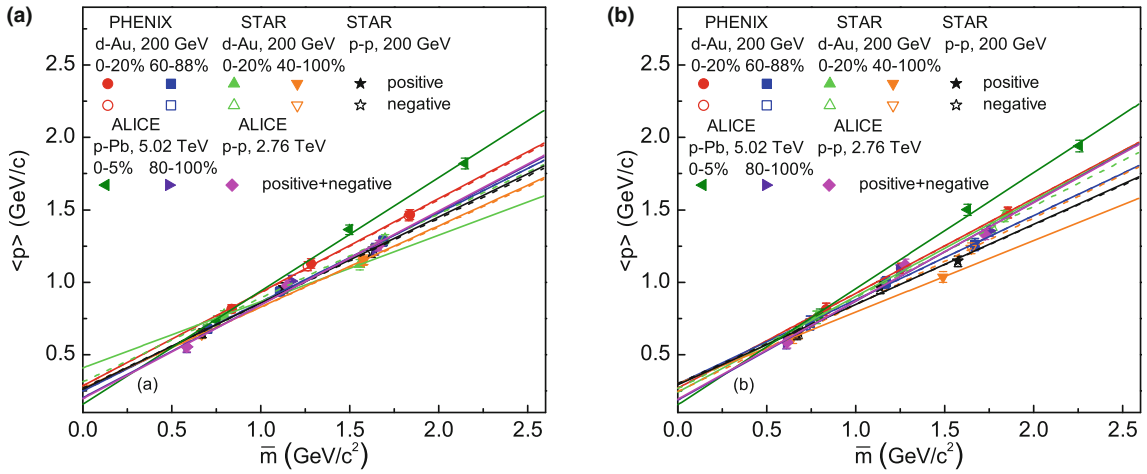

Fig. 7 (Color online) Relationship of $\langle p \rangle$ and $\overline{m}$. The symbols represent values of $\langle p \rangle$ for different $\overline{m}$ values, calculated from the parameters listed in Tables 3 and 4 and by an isotropic assumption in the rest frame of the emission source

by different collaborations is connected by scaling different amounts. The fit parameters are given in Tables 1, 2, 3, 4, where the values of N_0 are obtained from the scaled spectra, instead of the original spectra. It can be seen that the four considered models approximately describe the p_T spectra of the identified particles produced in the central (0–20%) and peripheral (40–94%) Cu–Cu collisions at $\sqrt{s_{NN}} = 200$ GeV.

Figures 9a and b show the relationships of T and m_0, as well as $\langle p_T \rangle$ and $\overline{m}$ ($\langle p \rangle$ and $\overline{m}$), according to the parameter values of Cu–Cu collisions at $\sqrt{s_{NN}} = 200$ GeV. It can be seen that the mentioned relationships show nearly linear tendencies in most cases. In particular, the intercept in Fig. 9a represents T_0, and the slopes related to $\langle p_T \rangle$ and $\langle p \rangle$ in Fig. 9b represent β_T and β, respectively.

For a qualitative comparison of the results obtained in different types of collisions, Tables 1 and 2, as well as Figs. 5, 6, and 9 are examined by comparing with the values of T_0 and β_T. It can be seen that the T_0 values in central Cu–Cu collisions are slightly smaller than those in central d–Au (or p–Pb) collisions because the size of Cu is smaller than that of Au (or Pb). This is a direct and strong evidence for the statement that the heaviest nucleus needs to be considered instead of the total nucleus to determine T_0. In addition, the T_0 in peripheral Cu–Cu collisions are nearly equal to those in peripheral d–Au (p–Pb) collisions and in pp collisions. Apparently, the dependence of β_T on the size of heaviest nucleus is undefined; however, β_T in central collisions is comparable with that in peripheral collisions.

The good agreement of the results obtained in the small system and nucleus–nucleus collisions reveal certain universalities in the hadroproduction process, as it is demonstrated in Refs. [31–35]. The universality in the

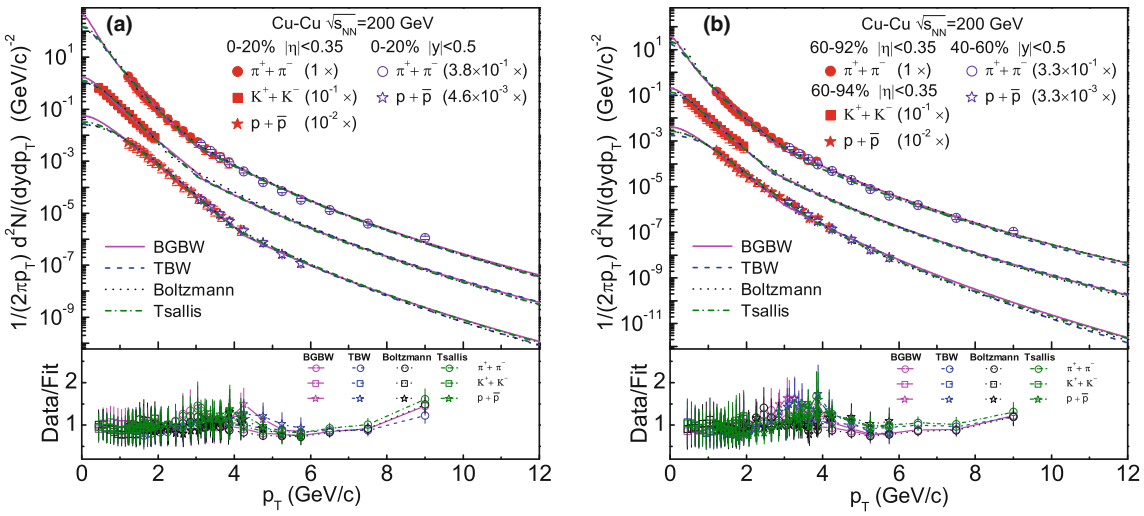

Fig. 8 (Color online) Spectra of $\pi^+ + \pi^-$, $K^+ + K^-$, and $p + \bar{p}$ produced in 0–20% (panel a) and 40–94% (panel b) Cu–Cu collisions at $\sqrt{s_{NN}} = 200$ GeV. The closed and open symbols represent the experimental data of the PHENIX and STAR collaborations measured in $|\eta| < 0.35$ and $|y| < 0.5$, respectively [29, 30], where the data in 0–20% was obtained by combining different centralities (0–5%, 5–10%, and 10–20%) to match with those in Fig. 1, and the data measured by different collaborations is connected by scaling the different amounts

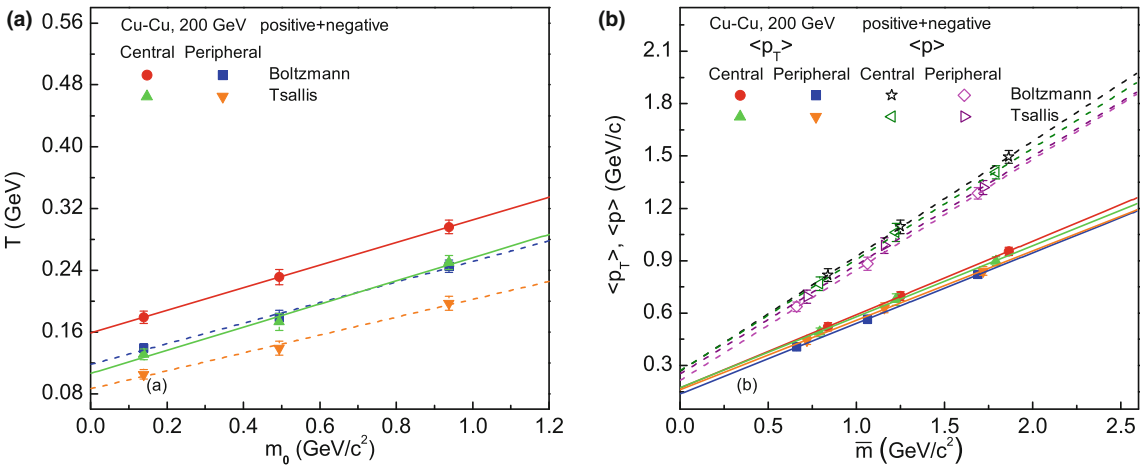

Fig. 9 (Color online) Relationship of T and m_0 (panel a), as well as $\langle p_T \rangle$ and $\overline{m}$ ($\langle p \rangle$ and $\overline{m}$) (panel b), according to the parameter values of Cu–Cu collisions at $\sqrt{s_{NN}} = 200$ GeV

hadroproduction process appears in different quantities observed [36] in different types of collisions (including proton–proton, proton–nucleus, and nucleus–nucleus collisions) and/or at different energies (available in the range from SPS BES to LHC) [31–35]. These quantities include, but not limited to mean multiplicity, rapidity or pseudorapidity density, multiplicity or transverse momentum distribution, and event patterns in different spaces under certain conditions. The present work confirms that the universality in the hadroproduction process possibly exists in thermal parameters at kinetic freeze-out in different types of collisions ranging from RHIC to LHC energies [14].

Although the blast-wave model and the related distributions have no contributions from resonance decays and strong stopping effects, a two-component form can be used to describe the spectra in very low and low p_T ranges. In addition, in d–Au and p–Pb collisions, the cold nuclear modification effects on the p_T spectra are not considered by us; however, a few of them widening the p_T spectra of the identified particles due to the multiple cascade collisions in the cold spectator region. If the contribution of the effects of cold nuclear modification on the p_T spectra is excluded, smaller T_0 and β_T can be obtained. The comparison with pp collisions reveals that the contribution of cold nuclear modification effects on T_0 and β_T is not obvious because peripheral nuclear collisions and pp collisions have similar

values. Furthermore, the contribution of cold nuclear modification effects on T_0 and β_T in Au–Au (Pb–Pb) collisions at the RHIC (LHC) is not obvious as well [14].

The Tsallis function is connected to the thermal model via its fits to the two- or three-component Boltzmann distribution [37]. Index q represents the degree of non-equilibrium among two or three states described by Boltzmann distributions, and the Tsallis temperature describes the fluctuations of Boltzmann temperatures. These explanations on the level of drawing curves of p_T reveal that the interacting systems at the RHIC and LHC stays in a transitional region from the extensive system to the non-extensive system. There is no obvious boundary to distinguish the extensive system and the non-extensive system for a given interacting system in the considered energy range. Nevertheless, at the RHIC and its beam energy scan energies or similar energies, the generic axiomatic non-extensive statistics is used to obtain the chemical freeze-out temperature and the baryon chemical potential [38–40]. This indicates that the Boltzmann–Gibbs and Tsallis statistics are not always necessary or applicable, which suggests that the interacting systems at the considered energies are complex, and more studies are needed in the future.

In central collisions at RHIC and LHC energies, the kinetic freeze-out temperature obtained from the four models is $T_0 \approx 120$ MeV. It is lower than the chemical freeze-out temperature $T_{ch} \approx 160$ MeV [1–4]. This confirms that the kinetic freeze-out occurs later than the chemical freeze-out at the considered energies. As an approximate treatment, we consider an ideal fluid, in which the time-evolution of the temperature follows $T_f = T_i(\tau_i/\tau_f)^{1/3}$, where T_i and τ_i are the initial temperature and proper time, respectively [41, 42], and T_f and τ_f denote the final temperature and time, respectively. When considering $T_i = 300$ MeV and $\tau_i = 1$ fm [42], the chemical freeze-out occurs at $\tau_{ch} \approx 6.6$ fm and the kinetic freeze-out occurs at $\tau_0 \approx 15.6$ fm. When considering peripheral collisions, the kinetic freeze-out occurs at $T_0 \approx 105$ MeV and $\tau_0 \approx 23.3$ fm. For instance, if a non-ideal fluid is considered, and the viscosity to entropy density ratio η/s is considered as 0.2, the time delay for the two freeze-outs is small, compared with the ideal fluid.

Let us summarize the main contributions of the present work as follows. Before reconsidering the first two models, applying a nearly zero β_T in them, the four models do not exhibit similar results. After reconsidering the first two models, applying a nonzero β_T in them, the four models exhibit similar results. By comparing the central nuclear collisions, the proton–proton collisions are found to be closer to the peripheral nuclear collisions, especially in terms of T_0 and β_T. The $T_0(\beta_T)$ value in the central collisions is comparable with that in the peripheral collisions, and $T_0(\beta_T)$ value in collisions at the LHC is comparable with that at the RHIC. At any rate, $T_0(\beta_T)$ value in the central collisions is not smaller than that in the peripheral collisions, and $T_0(\beta_T)$ value at the LHC is not smaller than that at the RHIC.

Before the final conclusions, it should be emphasized that the comparisons of different models and the obtained T_0 and β_T values in small collision system presented in this study are significant and useful owing to the collective expansion in a small system [43]. This also indicates that a large β_T ($\sim 0.4c$) is applied in peripheral nuclear collisions and pp collisions. As we know, certain models [6–8, 44–52] are used to obtain T_0 and β_T, and it is difficult to obtain the similar results compared to others [53–59] from these models with the increase of quantities. Although the present work provides similar results to [53–59] by the four models, the first and third models are preferred as they use a Boltzmann distribution, which is closer to the well-known ideal gas model. In addition, the hard component has no contribution to T_0 and β_T due to its non-thermal production. Instead, the very soft and soft components, which contribute fitly in the very low and low p_T regions, are used to obtain T_0 and β_T. Thus, the third and fourth fits are suitable, because they can be applied for massive particles and in very low and low p_T ranges.

In addition, complex physics processes, high-energy collisions contain abundant information. This information includes, but is not limited to, electromagnetic field effects [60], strong magnetic field effects [61], and particular effects of strangeness [62]. The determination of T_0 and β_T can be affected by these effects; hence, the search for the QCD critical point [63]. As a study at the exploratory stage of development, the present work still has needs to be improved with the highest possible accuracy. Further studies needs to be focused on the accurate determinations of T_0 and β_T. In addition, the accurate determination of other types of temperatures, such as the effective temperature, chemical freeze-out temperature, and initial temperature, and comparisons of their dependences on the centrality and collision energy is also in the focus of our research.

4 Conclusion

As a conclusion, the transverse momentum distributions of π^+, π^-, K^+, K^-, p, and $\bar{p}$ produced in pp and d–Au collisions at the RHIC, as well as in pp and p–Pb collisions at the LHC, have been analyzed by four models. The first two models utilize the blast-wave model with Boltzmann–Gibbs statistics and with Tsallis statistics, respectively. The

last two models employ certain linear correspondences, in which the Boltzmann and Tsallis distributions are used to obtain the effective temperatures. These models and distributions describe only the contribution of the soft excitation process. For the hard scattering process, the inverse power law is uniformly used.

The experimental data measured by the PHENIX, STAR, and ALICE collaborations is fitted by the model results. We used a nonzero β_T in the first two methods. The four models present similar results. Both T_0 and β_T in central collisions are comparable with those in peripheral collisions. With the increase of collision energy ranging from that of the RHIC to that of the LHC, the considered quantities typically do not decrease. Comparing with the central nuclear collisions, the *pp* collisions are closer to the peripheral nuclear collisions. In nuclear collisions, the excitation degree at the kinetic freeze-out is mainly determined by the heaviest nucleus and collision energy.

Acknowledgements We highly appreciate the communications with Dr. Muhammad Waqas.

References

1. J. Cleymans, H. Oeschler, K. Redlich et al., Comparison of chemical freeze-out criteria in heavy-ion collisions. Phys. Rev. C **73**, 034905 (2006). https://doi.org/10.1103/PhysRevC.73.034905
2. A. Andronic, P. Braun-Munzinger, J. Stachel, Hadron production in central nucleus–nucleus collisions at chemical freeze-out. Nucl. Phys. A **772**, 167 (2006). https://doi.org/10.1016/j.nuclphysa.2006.03.012
3. A. Andronic, P. Braun-Munzinger, J. Stachel, Thermal hadron production in relativistic nuclear collisions. Acta Phys. Pol. B **40**, 1005 (2009). arXiv:0901.2909 [nucl-th]
4. A. Andronic, P. Braun-Munzinger, J. Stachel, The horn, the hadron mass spectrum and the QCD phase diagram—the statistical model of hadron production in central nucleus-nucleus collisions. Nucl. Phys. A **834**, 237c (2010). https://doi.org/10.1016/j.nuclphysa.2009.12.048
5. S. Chatterjee, S. Das, L. Kumar et al., Freeze-out parameters in heavy-ion collisions at AGS, SPS, RHIC, and LHC energies. Adv. High Energy Phys. **2015**, 349013 (2015). https://doi.org/10.1155/2015/349013
6. E. Schnedermann, J. Sollfrank, U. Heinz, Thermal phenomenology of hadrons from 200*A* GeV S+S collisions. Phys. Rev. C **48**, 2462 (1993). https://doi.org/10.1103/PhysRevC.48.2462
7. B.I. Abelev et al., (STAR Collaboration), Systematic measurements of identified particle spectra in pp, d+Au, and Au+Au collisions at the STAR detector. Phys. Rev. C **79**, 034909 (2009). https://doi.org/10.1103/PhysRevC.79.034909
8. B.I. Abelev et al., (STAR Collaboration), Identified particle production, azimuthal anisotropy, and interferometry measurements in Au+Au collisions at $\sqrt{s_{NN}} = 9.2$ GeV. Phys. Rev. C **81**, 024911 (2010). https://doi.org/10.1103/PhysRevC.81.024911
9. Z.B. Tang, Y.C. Xu, L.J. Ruan et al., Spectra and radial flow in relativistic heavy ion collisions with Tsallis statistics in a blast-wave description. Phys. Rev. C **79**, 051901(R) (2009). https://doi.org/10.1103/PhysRevC.79.051901
10. S. Takeuchi, K. Murase, T. Hirano et al., Effects of hadronic rescattering on multistrange hadrons in high-energy nuclear collisions. Phys. Rev. C **92**, 044907 (2015). https://doi.org/10.1103/PhysRevC.92.044907
11. H. Heiselberg, A.M. Levy, Elliptic flow and Hanbury–Brown–Twiss in noncentral nuclear collisions. Phys. Rev. C **59**, 2716 (1999). https://doi.org/10.1103/PhysRevC.59.2716
12. U.W. Heinz, *Lecture Notes for Lectures Presented at the 2nd CERN-Latin-American School of High-Energy Physics, June 1–14, 2003* (San Miguel Regla, Mexico, 2004). arXiv:hep-ph/0407360
13. R. Russo, Measurement of D^+ meson production in p–Pb collisions with the ALICE detector, Ph.D. thesis (Universita degli Studi di Torino, Italy, 2015). arXiv:1511.04380 [nucl-ex]
14. H.-L. Lao, F.-H. Liu, B.-C. Li, Kinetic freeze-out temperatures in central and peripheral collisions: which one is larger? Nucl. Sci. Tech. **29**, 82 (2018). https://doi.org/10.1007/s41365-018-0425-x
15. H.-R. Wei, F.-H. Liu, R.A. Lacey, Kinetic freeze-out temperature and flow velocity extracted from transverse momentum spectra of final-state light flavor particles produced in collisions at RHIC and LHC. Eur. Phys. J. A **52**, 102 (2016). https://doi.org/10.1140/epja/i2016-16102-6
16. H.-L. Lao, H.-R. Wei, F.-H. Liu, An evidence of mass-dependent differential kinetic freeze-out scenario observed in Pb–Pb collisions at 2.76 TeV. Eur. Phys. J. A **52**, 203 (2016). https://doi.org/10.1140/epja/i2016-16203-2
17. H.-R. Wei, F.-H. Liu, R.A. Lacey, Disentangling random thermal motion of particles and collective expansion of source from transverse momentum spectra in high energy collisions. J. Phys. G **43**, 125102 (2016). https://doi.org/10.1088/0954-3899/43/12/125102
18. J. Cleymans, D. Worku, Relativistic thermodynamics: transverse momentum distributions in high-energy physics. Eur. Phys. J. A **48**, 160 (2012). https://doi.org/10.1140/epja/i2012-12160-0
19. H. Zheng, L.L. Zhu, Comparing the Tsallis distribution with and without thermodynamical description in p+p collisions. Adv. High Energy Phys. **2016**, 9632126 (2016). https://doi.org/10.1155/2016/9632126
20. A. Adare et al., (PHENIX Collaboration), Spectra and ratios of identified particles in Au+Au and d+Au collisions at $\sqrt{s_{NN}} =$ 200 GeV. Phys. Rev. C **88**, 024906 (2013). https://doi.org/10.1103/PhysRevC.88.024906
21. J. Adams et al., (STAR Collaboration), Identified hadron spectra at large transverse momentum in p+p and d+Au collisions at $\sqrt{s_{NN}} = 200$ GeV. Phys. Lett. B **637**, 161 (2006). https://doi.org/10.1016/j.physletb.2006.04.032
22. G. Agakishiev et al., (STAR Collaboration), Identified hadron compositions in p+p and Au+Au collisions at high transverse momenta at $\sqrt{s_{NN}} =$ 200 GeV. Phys. Rev. Lett. **108**, 072302 (2012). https://doi.org/10.1103/PhysRevLett.108.072302
23. J. Adams, (STAR Collaboration), Pion, kaon, proton and anti-proton transverse momentum distributions from p+p and d+Au collisions at $\sqrt{s_{NN}} =$ 200 GeV. Phys. Lett. B **616**, 8 (2005). https://doi.org/10.1016/j.physletb.2005.04.041
24. J. Adam et al., (ALICE Collaboration), Multiplicity dependence of charged pion, kaon, and (anti)proton production at large transverse momentum in p–Pb collisions at $\sqrt{s_{NN}} = 5.02$ TeV. Phys. Lett. B **760**, 720 (2016). https://doi.org/10.1016/j.physletb.2016.07.050
25. B. Abelev et al., (ALICE Collaboration), Production of charged pions, kaons and protons at large transverse momenta in *pp* and Pb–Pb collisions at $\sqrt{s_{NN}} = 2.76$ TeV. Phys. Lett. B **736**, 196 (2014). https://doi.org/10.1016/j.physletb.2014.07.011

26. R. Odorico, Does a transverse energy trigger actually trigger on large-p_T jets? Phys. Lett. B **118**, 151 (1982). https://doi.org/10.1016/0370-2693(82)90620-7
27. G. Arnison et al., (UA1 Collaboration), Transverse momentum spectra for charged particles at the CERN proton–antiproton collider. Phys. Lett. B **118**, 167 (1982). https://doi.org/10.1016/0370-2693(82)90623-2
28. T. Mizoguchi, M. Biyajima, N. Suzuki, Analyses of whole transverse momentum distributions in $p\bar{p}$ and pp collisions by using a modified version of Hagedorn's formula. Int. J. Mod. Phys. A **32**, 1750057 (2017). https://doi.org/10.1142/S0217751X17500579
29. http://www.phenix.bnl.gov/WWW/show_plot.php.html, quoted from ref. [19] (which shows the web page) in P. Guptaroy, G. Sau, S.K. Biswas, S. Bhattacharyya, Understanding the characteristics of multiple production of light hadrons in Cu+Cu interactions at various RHIC energies: a model-based analysis. Nuovo Cimento B **125**, 1071 (2010). 10.1393/ncb/i2010-10913-4, arXiv:0907.2008v2 [hep-ph]
30. B.I. Abelev et al., (STAR Collaboration), Spectra of identified high-$p_T\pi^{\pm}$ and p(p) in Cu+Cu collisions at $\sqrt{s_{\rm NN}} = 200$ GeV. Phys. Rev. C **81**, 054907 (2010). https://doi.org/10.1103/PhysRevC.81.054907
31. E.K.G. Sarkisyan, A.S. Sakharov, Multihadron production features in different reactions. AIP Conf. Proc. **828**, 35 (2006). https://doi.org/10.1063/1.2197392
32. E.K.G. Sarkisyan, A.S. Sakharov, Relating multihadron production in hadronic and nuclear collisions. Eur. Phys. J. C **70**, 533 (2010). https://doi.org/10.1140/epjc/s10052-010-1493-1
33. A.N. Mishra, R. Sahoo, E.K.G. Sarkisyan, Effective-energy budget in multiparticle production in nuclear collisions. Eur. Phys. J. C **74**, 3147 (2014). https://doi.org/10.1140/epjc/s10052-015-3275-2. and Erratum. Eur. Phys. J. C **75** 70 (2015). https://doi.org/10.1140/epjc/s10052-014-3147-1
34. E.K.G. Sarkisyan, A.N. Mishra, R. Sahoo et al., Multihadron production dynamics exploring the energy balance in hadronic and nuclear collisions. Phys. Rev. D **93**, 054046 (2016). https://doi.org/10.1103/PhysRevD.93.054046 and Addendum. Phys. Rev. D **93**, 079904 (2016). https://doi.org/10.1103/PhysRevD.93.079904
35. E.K.G. Sarkisyan, A.N. Mishra, R. Sahoo et al., Centrality dependence of midrapidity density from GeV to TeV heavy-ion collisions in the effective-energy universality picture of hadroproduction. Phys. Rev. D **94**, 011501(R) (2016). https://doi.org/10.1103/PhysRevD.94.011501
36. C. Patrignani et al., (Particle data group), Review of particle physics. Chin. Phys. C **40**, 100001 (2016). https://doi.org/10.1088/1674-1137/40/10/100001
37. F.-H. Liu, Y.-Q. Gao, B.-C. Li, Comparing two-Boltzmann distribution and Tsallis statistics of particle transverse momentums in collisions at LHC energies. Eur. Phys. J. A **50**, 123 (2014). https://doi.org/10.1140/epja/i2014-14123-9
38. A.N. Tawfik, Axiomatic nonextensive statistics at NICA energies. Eur. Phys. J. A **52**, 253 (2016). https://doi.org/10.1140/epja/i2016-16253-4
39. A.N. Tawfik, H. Yassin, E.R.A. Elyazeed, On thermodynamic self-consistency of generic axiomatic-nonextensive statistics. Chin. Phys. C **41**, 053107 (2017). https://doi.org/10.1088/1674-1137/41/5/053107
40. A.N. Tawfik, Lattice QCD thermodynamics and RHIC-BES particle production within generic nonextensive statistics. Phys. Part. Nucl. Lett. (PEPAN) **15**, 199 (2018). https://doi.org/10.1134/S1547477118030196
41. J.D. Bjorken, Highly relativistic nucleus–nucleus collisions: the central rapidity region. Phys. Rev. D **27**, 140 (1983). https://doi.org/10.1103/PhysRevD.27.140
42. K. Okamoto, C. Nonaka, A new relativistic viscous hydrodynamics code and its application to the Kelvin–Helmholtz instability in high-energy heavy-ion collisions. Eur. Phys. J. C **77**, 383 (2017). https://doi.org/10.1140/epjc/s10052-017-4944-0
43. H.C. Song, Y. Zhou, K. Gajdošová, Collective flow and hydrodynamics in large and small systems at the LHC. Nucl. Sci. Tech. **28**, 99 (2017). https://doi.org/10.1007/s41365-017-0245-4
44. S. Das (for the STAR Collaboration), Identified particle production and freeze-out properties in heavy-ion collisions at RHIC beam energy scan program. EPJ Web Conf. **90**, 08007 (2015). https://doi.org/10.1051/epjconf/20159008007
45. S. Das (for the STAR Collaboration), Centrality dependence of freeze-out parameters from the beam energy scan at STAR. Nucl. Phys. A **904–905**, 891c (2013). https://doi.org/10.1016/j.nuclphysa.2013.02.158
46. L. Adamczyk et al., (STAR Collaboration), Bulk properties of the medium produced in relativistic heavy-ion collisions from the beam energy scan program. Phys. Rev. C **96**, 044904 (2017). https://doi.org/10.1103/PhysRevC.96.044904
47. X.F. Luo, Exploring the QCD phase structure with beam energy scan in heavy-ion collisions. Nucl. Phys. A **956**, 75 (2016). https://doi.org/10.1016/j.nuclphysa.2016.03.025
48. C. Markert (for the STAR Collaboration), Resonance production in heavy-ion collisions at STAR. J. Phys. G **35**, 044029 (2008). https://doi.org/10.1088/0954-3899/35/4/044029
49. I. Melo, B. Tomášik, Reconstructing the final state of Pb+Pb collisions at $\sqrt{s_{\rm NN}} = 2.76$. TeV. J. Phys. G **43**, 015102 (2016). https://doi.org/10.1088/0954-3899/43/1/015102
50. A. Iordanova, (for the STAR Collaboration), Strangeness and bulk freeze-out properties at RHIC. J. Phys. G **35**, 044008 (2008). https://doi.org/10.1088/0954-3899/35/4/044008
51. A. Iordanova, (for the STAR Collaboration), O. Barannikova, R. Hollis, System size dependence of freeze-out properties at RHIC. Int. J. Mod. Phys. E **16**, 1800 (2007). https://doi.org/10.1142/S0218301307007027
52. A. Ortiz, G. Bencédi, H. Bello, Revealing the source of the radial flow patterns in proton–proton collisions using hard probes. J. Phys. G **44**, 065001 (2017). https://doi.org/10.1088/1361-6471/aa6594
53. S.S. Adler et al., (PHENIX Collaboration), Identified charged particle spectra and yields in Au+Au collisions at $\sqrt{s_{NN}} = 200$ GeV. Phys. Rev. C **69**, 034909 (2004). https://doi.org/10.1103/PhysRevC.69.034909
54. S. Chatterjee, B. Mohanty, R. Singh, Freezeout hypersurface at energies available at the CERN large hadron collider from particle spectra: flavor and centrality dependence. Phys. Rev. C **92**, 024917 (2015). https://doi.org/10.1103/PhysRevC.92.024917
55. Z.B. Tang, L. Yi, L.J. Ruan et al., The statistical origin of constituent-quark scaling in the QGP hadronization. Chin. Phys. Lett. **30**, 031201 (2013). https://doi.org/10.1088/0256-307X/30/3/031201
56. K. Jiang, Y.Y. Zhu, W.T. Liu et al., Onset of radial flow in p+p collisions. Phys. Rev. C **91**, 024910 (2015). https://doi.org/10.1103/PhysRevC.91.024910
57. B. De, Non-extensive statistics and understanding particle production and kinetic freeze-out process from p_T-spectra at 2.76 TeV. Eur. Phys. J. A **50**, 138 (2014). https://doi.org/10.1140/epja/i2014-14138-2
58. D. Thakur, S. Tripathy, P. Garg, et al., Proceedings of the 11th Workshop on Particle Correlations and Femtoscopy (WPCF 2015), Nov. 3–7 2015, (Warsaw, Poland, 2016). arXiv:1603.04971 [hep-ph]
59. D. Thakur, S. Tripathy, P. Garg et al., Indication of a differential freeze-out in proton-proton and heavy-ion collisions at RHIC and LHC energies. Adv. High Energy Phys. **2016**, 4149352 (2016). https://doi.org/10.1155/2016/4149352

60. X.-G. Deng, Y.-G. Ma, Electromagnetic field effects on nucleon transverse momentum for heavy ion collisions around 100 A MeV. Nucl. Sci. Tech. **28**, 182 (2017). https://doi.org/10.1007/s41365-017-0337-1
61. K. Hattori, X.-G. Huang, Novel quantum phenomena induced by strong magnetic fields in heavy-ion collisions. Nucl. Sci. Tech. **28**, 26 (2017). https://doi.org/10.1007/s41365-016-0178-3
62. W.-Z. Jiang, R.-Y. Yang, S.-N. Wei, Strangeness to increase the density of finite nuclear systems in constraining the high-density nuclear equation of state. Nucl. Sci. Tech. **28**, 180 (2017). https://doi.org/10.1007/s41365-017-0333-5
63. X.-F. Luo, N. Xu, Search for the QCD critical point with fluctuations of conserved quantities in relativistic heavy-ion collisions at RHIC: an overview. Nucl. Sci. Tech. **28**, 112 (2017). https://doi.org/10.1007/s41365-017-0257-0